



HAL
open science

Understanding the Dust Environment at Mercury: From Surface to Exosphere

Harald Krüger, Michelle S Thompson, Masanori Kobayashi, Valeria Mangano, Martina Moroni, Anna Milillo, Lindsay P Keller, Sho Sasaki, Joe Zender, Deborah Domingue, et al.

► To cite this version:

Harald Krüger, Michelle S Thompson, Masanori Kobayashi, Valeria Mangano, Martina Moroni, et al.. Understanding the Dust Environment at Mercury: From Surface to Exosphere. *The Planetary Science Journal*, 2024, 5, pp.36. 10.3847/psj/ad11f5 . insu-04458810

HAL Id: insu-04458810

<https://insu.hal.science/insu-04458810>





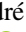




Submitted on 15 Feb 2024

HAL is a multi-disciplinary open access archive for the deposit and dissemination of scientific research documents, whether they are published or not. The documents may come from teaching and research institutions in France or abroad, or from public or private research centers.

L'archive ouverte pluridisciplinaire **HAL**, est destinée au dépôt et à la diffusion de documents scientifiques de niveau recherche, publiés ou non, émanant des établissements d'enseignement et de recherche français ou étrangers, des laboratoires publics ou privés.



Understanding the Dust Environment at Mercury: From Surface to Exosphere

Harald Krüger¹, Michelle S. Thompson^{2,14} , Masanori Kobayashi³, Valeria Mangano⁴ , Martina Moroni⁴, Anna Milillo⁴ ,
Lindsay P. Keller⁵ , Sho Sasaki⁶, Joe Zender⁷, Deborah Domingue⁸ , Johannes Benkhoff⁷, André Galli⁹ ,
François LeBlanc¹⁰ , Go Murakami¹¹, Menelaos Sarantos¹² , and Daniel W. Savin¹³ 

¹Max-Planck-Institut für Sonnensystemforschung, Justus-von-Liebig-Weg 3, D-37077 Göttingen, Germany

²Department of Earth, Atmospheric, and Planetary Sciences, Purdue University, 550 Stadium Mall Drive, West Lafayette, IN 47907, USA

³Planetary Exploration Research Center, Chiba Institute of Technology, Narashino, Chiba, 275-0016, Japan

⁴Institute for Astrophysics and Planetology from Space, Rome, Italy

⁵ARES, Mail Code XI3, NASA Johnson Space Center, 2101 NASA Parkway, Houston, TX 77058, USA

⁶Department of Earth and Space Science, Osaka University, Toyonaka, Osaka, 560-0043, Japan

⁷ESA, ESTEC, Netherlands

⁸Planetary Science Institute, Tucson, AZ 85719-2395, USA

⁹Space Research and Planetary Sciences, Physics Institute, University of Bern, Switzerland

¹⁰LATMOS/CNRS, Sorbonne University, Paris, France

¹¹ISAS, JAXA, Japan

¹²NASA Goddard Space Flight Center, Greenbelt, MD 20771, USA

¹³Columbia Astrophysics Laboratory, Columbia University, 538 West 120th Street, New York, NY 10027, USA

Received 2023 October 1; revised 2023 November 22; accepted 2023 November 30; published 2024 February 12

Abstract

We provide an overview of our understanding of the dust environment at Mercury and the role that dust plays in shaping the planet's surface and exosphere. Our understanding of the role that dust impacts play in the generation of Mercury's atmosphere has evolved considerably with continued analysis of results from the MERcury SURface, SPACE ENvironment, GEochemistry, and RANGing (MESSENGER) mission. Recent models have provided evidence for the probable release of refractory species into Mercury's exosphere via impacts. However, there remain significant questions regarding the relative contributions of atoms released via impacts versus other mechanisms (e.g., photon-stimulated desorption) to the overall exospheric budget. We also discuss the state of observational and modeling efforts to constrain the dust environment at Mercury, including sources from the zodiacal cloud, cometary trails, and interstellar dust. We describe the advancements that will be made in our characterization of dust at Mercury with BepiColombo, providing observational constraints on the dust clouds themselves and the role that impacts play in exospheric generation. On Mercury's surface, there remain outstanding questions regarding the role that dust impacts play in the regolith cycling and development. We review how improved modeling efforts to understand grain lifetimes as a function of impactor flux will further our understanding of Mercury's regolith. Finally, there are few constraints on the role of dust impacts on the space weathering of Mercury's surface, particularly the expected chemical, physical, and spectral alterations to the regolith. Here we discuss the importance of laboratory experiments to simulate these processes for the interpretation of data from MESSENGER and BepiColombo.

Unified Astronomy Thesaurus concepts: Mercury (planet) (1024); Zodiacal cloud (1845); Exosphere (499); Impact gardening (2299); Dust composition (2271)

1. Introduction

One of the earliest known phenomena caused by interplanetary dust is the zodiacal light, sunlight scattered by dust particles orbiting the Sun. The lifetimes of individual dust particles in interplanetary space are much shorter than the age of the solar system (Grün et al. 1985), implying that interplanetary dust must have contemporary sources, namely, bigger objects like meteoroids, comets, and asteroids, as well as planetary moons and rings. In addition, dust particles immersed in the Local Interstellar Cloud, through which the solar system currently passes, penetrate the planetary system (Grün et al. 1994; Mann 2010; Sterken et al. 2019 and references therein). Typically, interstellar dust moves through the solar system on

unbound, hyperbolic trajectories. Dust can have different characteristics in different regions of the solar system. It consists not only of refractory rocky or metallic material, as in stony and iron meteorites, but also of carbonaceous material; dust in the outer solar system can even be ice particles (Hsu et al. 2015; Khawaja et al. 2019).

Different methods are available to study dust in interplanetary space. These are distinguished by the size or mass range of the particles to be studied (Fechtig et al. 2001; Grün et al. 2019; Koschny et al. 2019; Janches et al. 2021 and references therein). The earliest methods were ground-based zodiacal light and meteor observations, with radar observations of meteor trails becoming available much later. With the advent of spaceflight, in situ detection by space instrumentation provided new information on small dust particles. Modern impact-ionization detectors allow not only for the detection and measurement of particle mass and impact speed, but also for the chemical analysis of dust particles in space (Srama et al. 2004; Kempf 2018; Kobayashi et al. 2018). Deep-space probes equipped with dust detectors identified space dust from 0.3 au

¹⁴ Corresponding author



out to 50 au from the Sun (Bernardoni et al. 2022). In addition to dedicated calibrated dust detectors and analyzers, dust particle impacts onto spacecraft were also recorded with plasma instruments (Gurnett et al. 1983; Meyer-Vernet et al. 2009; Szalay et al. 2021). Measurements with plasma instruments may benefit from the larger sensitive areas as compared to dedicated in situ dust instruments, however, they remain largely uncalibrated because particle masses and impact speeds are difficult to determine, and compositional measurements are not possible.

Natural (lunar, asteroidal, and cometary) samples and artificial surfaces exposed to micrometeoroid impacts have been returned from space and analyzed (note that here “dust” and “micrometeoroid” are used synonymously). High-flying aircraft collected dust in the stratosphere that was identified as extraterrestrial material and was analyzed in the laboratory with the most advanced microanalytic tools. On Earth, micrometeorites were extracted from snow fields on the polar caps, and, more recently, even collected on rooftops (Larsen & Genge 2016; Jonker et al. 2023). Finally, modern space-based infrared observatories allow for the observation of the thermal emission from interplanetary dust in the outer solar system. Beyond our solar system, hundreds of so-called debris disks were identified around other stars by their emission at infrared and longer wavelengths. They are natural dust disks, forming the extrasolar counterparts of our own zodiacal dust cloud. Recent reviews on these topics were given by Hughes et al. (2018), Koschny et al. (2019), and Grün et al. (2019).

In the inner solar system, the first in situ dust measurements were performed by the two Helios spacecraft in the 1970s. The spacecraft reached an orbital perihelion at 0.3 au from the Sun, well within the orbit of the innermost planet, Mercury. Both spacecraft were equipped with zodiacal light photometers and in situ dust sensors, the latter of which measured the distribution of interplanetary and interstellar dust in the inner solar system for the first time (Grün et al. 1980; Altobelli et al. 2006). The zodiacal light photometer on board Helios discovered a heliocentric dust ring along Venus’ orbit (Leinert & Moster 2007), which was later confirmed by the Heliospheric Imager instruments on board the two Solar TERrestrial RELations Observatory spacecraft (STEREO; Jones et al. 2013). From the STEREO observations, the enhancement in the dust spatial density in the Venus ring with respect to the interplanetary dust background was found to be only 8% at most (Jones 2017). A similar but fainter dust ring was also suggested to exist along Mercury’s orbit with an enhancement in the dust density of only 10% (Stenborg et al. 2021), although the stability of this ring was put into question by theoretical considerations (Sommer et al. 2020). Yet closer to the Sun, the solar F-corona arises from photospheric light scattering off the zodiacal dust (Mann et al. 2004 and references therein). The region close to the Sun was theoretically predicted to be dust free (e.g., Mukai et al. 1974), and observations with the Parker Solar Probe recently confirmed a decrease in the intensity of the F-coronal intensity (Howard et al. 2019). Finally, the plasma instrument on board the Parker Solar Probe has detected dust impacts as close as 30 solar radii away from the Sun (Malaspina et al. 2022).

In the inner solar system, dust destruction due to particle heating and collisions likely becomes a major player affecting the zodiacal dust density (Szalay et al. 2021). Compared to the rich dust environments of the giant planets, in particular Jupiter and Saturn (Krüger et al. 2004; Srama et al. 2011;

Spahn et al. 2019), dust around the inner terrestrial planets Mercury and Venus is much more tenuous because of the absence of moons that could act as dust sources. Among these two planets, only Mercury is expected to be surrounded by a faint dust cloud created by interplanetary impactors (Müller et al. 2002) because it lacks a significant atmosphere.

Dust grains can be generated by endogenic and exogenic processes (e.g., Szalay et al. 2018 and references therein). All celestial bodies without gaseous atmospheres are permanently exposed to bombardment by hypervelocity micrometeoroids (speeds in excess of 3 km s^{-1}), which knock-off ejecta dust particles from the surfaces of these bodies (impact-ejecta mechanism). This process leads to impact vaporization of surface material and surface alteration (gardening). Collisions between macroscopic bodies also release dust, for example in the asteroid belt (Sykes & Greenberg 1986), and in Saturn’s main rings (Spahn et al. 2019). Endogenic processes include dust release from active comets and (cryo-)volcanic plumes (on Enceladus and Io).

The forces dominating particle dynamics are strongly grain-size dependent. Once released from their parent body, dust particles collect an electric charge (Horanyi 1996), making them susceptible to electromagnetic forces. In particular, the streams of tiny electromagnetically interacting grains or dust ejected from the Jovian and the Saturnian systems into interplanetary space are strongly affected by the solar wind and its structures, like corotating interaction regions and coronal mass ejections (Flandes et al. 2011; Hsu et al. 2012). In general, the most important forces in the interplanetary environment are typically the gravity of the Sun, the electromagnetic force, solar radiation pressure, plasma drag, and Poynting–Robertson drag (e.g., Horanyi 1996; Kimura & Mann 1999; Dermott et al. 2001; Nesvorný et al. 2011a). Circumplanetary dust is generally confined to the planetary environment, although dust streams emanating from the Jovian and Saturnian systems are a (minor) source of interplanetary and interstellar dust as well (Hsu et al. 2012). In the inner solar system, Parker Solar Probe observations indicate that collisional erosion of dust within 10–20 solar radii suggests the existence of nanograins with radii below approximately 50 nm, which are susceptible to electromagnetic forces, and somewhat larger particles on hyperbolic trajectories escaping the solar system driven by solar radiation pressure (β meteoroids; Szalay et al. 2020; Mann & Czechowski 2021; Szalay et al. 2021; Zaslavsky et al. 2021).

In the 1970s, Mercury was the target of the Mariner 10 spacecraft (Giberson & Cunningham 1975; Strom 1979), and between 2011 and 2015 the MERcury Surface, Space ENVIRONMENT, GEOchemistry, and Ranging (MESSENGER) spacecraft was in orbit about the planet (Solomon et al. 2007, 2018). However, none of these spacecraft were equipped with an in situ dust detector. Nevertheless, observations performed with the UltraViolet and Visible Spectrometer (UVVS) and the Fast Imaging Plasma Spectrometer (FIPS) on board MESSENGER (Andrews et al. 2007) emphasized the significance of dust and meteoroid impacts for the formation of the Hermean exosphere: For example, seasonal variations and transient enhancements in the exospheric source rate of metallic constituents like calcium and magnesium were attributed to dust impacts (Burger et al. 2014; Christou et al. 2015; Killen & Hahn 2015; Pokorný 2018; Jasinski et al. 2020). To date, the best-studied impact-ejecta dust cloud is the one at the Moon (Szalay & Horanyi 2015a; Horanyi et al. 2015).

Here we review our present knowledge about dust in the inner solar system, with a special emphasis on the environment of Mercury, in light of the upcoming BepiColombo mission at Mercury (Benkhoff et al. 2010, 2021). Starting from the observational evidence provided by MESSENGER, which showed that dust plays a significant role in the formation of the Hermean exosphere (Section 2), we give an overview of the interplanetary dust environment to which our innermost planet Mercury is exposed (Section 3). Next, we review measurements of the impact-ejecta dust clouds at Jupiter’s Galilean moons and the Earth’s Moon and give a brief overview about the formation mechanisms of dust clouds surrounding airless celestial bodies (Section 4). In Section 5, we summarize our knowledge about electrostatic processes which may cause transport of electrically charged dust across the surfaces of these bodies. In Section 6, we review our knowledge about surface processes; and in Section 7, we discuss the expected corresponding effects on surface materials, including the microstructural and chemical products predicted in the surface regolith at Mercury. In Section 8, we summarize future laboratory and theoretical studies needed to better understand dust-related surface processes relevant to the formation and evolution of the Hermean exosphere.

2. Meteoroid Impacts as One Source of Mercury’s Exosphere

The exosphere is a thin, atmosphere-like structure surrounding a planet or natural satellite where molecules are gravitationally bound to the body, but where the density is so low that the molecules essentially do not collide with each other. In the case of bodies with substantial atmospheres, such as the Earth, the exosphere is the uppermost layer, where the atmosphere thins out and merges with outer space. In contrast, Mercury and several large natural satellites such as the Moon, Europa, and Ganymede have exospheres without a denser atmosphere underneath (called “surface-bounded exospheres”) and their exospheres are directly in contact with the surface. Hence, the surface acts as both a source and sink for exospheric molecules and the exospheric composition is strongly linked to the composition and structure of the surface. Several processes are believed to be likely source mechanisms for surface-bounded exospheres and space weathering of these surfaces, including thermal desorption, photon-stimulated and electron-stimulated desorption, and ion and chemical sputtering. The significance of each of these processes is still under debate (see, e.g., the reviews by Milillo et al. 2005; Domingue et al. 2014; Killen et al. 2018; Grava et al. 2021; Wurz et al. 2022; and the companion papers from this focus issue). A fraction of the volatiles released into the exosphere is produced also by regolith vaporization following hypervelocity impacts of (micro)meteoroids onto the planetary surface (e.g., Wurz et al. 2022). The continuous bombardment of the surface by micrometeoroids is also believed to be an important cause of the regolith gardening, i.e., the pulverization and overturn of the upper crust providing fresh material in the upper layers to be further released to the exosphere (Killen et al. 2018). Micrometeoroid impacts release ejecta, melt, and vapor. Impacts of larger projectiles (meteoroids) are much rarer but can excavate deeper layers, thereby exposing fresh material to the external environment and to eroding agents like solar radiation and ions.

Given the lack of direct measurements of micrometeoroids at Mercury, *N*-body numerical simulations of small particles have been performed to rescale the dust populations known to exist at the heliocentric distances of Earth to be applicable to Mercury. Mercury’s orbital asymmetry is predicted to result in a slightly higher impactor flux at aphelion than at perihelion and in a surface region at $\pm 40^\circ$ latitude (Borin et al. 2016a). Finally, a statistical analysis of the flux of micrometeoroids from cometary and asteroidal origins indicated a lower contribution due to the cometary component (Borin et al. 2016b), although this has recently been challenged (Section 3.1).

Kameda et al. (2009, 2011) suggested that the impact vaporization mainly originated from the dust distribution in the inner solar system. In that study, the intensification of global average exospheric sodium along Mercury’s eccentric and inclined orbit, as observed from Earth-based telescopes, appeared to be related to the passage through the interplanetary dust disk along the ecliptic. If so, the formation of the sodium exosphere would relate to the bombardment of the surface by interplanetary dust, although dust impact vaporization most likely plays a minor role as compared to photon-stimulated desorption and other processes in the global process of sodium exosphere generation (Killen et al. 2018; Wurz et al. 2022).

Nevertheless, recent data and models provide evidence that hypervelocity impacts of micrometeoroids and subsequent vaporization are important mechanisms for the release of exospheric atoms from Mercury’s surface (Killen et al. 2018; Janches et al. 2021). In fact, calcium and magnesium are two other refractory species in Mercury’s exosphere that have been studied more recently thanks to both observations from the Earth and especially in situ with MESSENGER’s Mercury Atmosphere and Surface Composition Spectrometer (MASCS) UltraViolet and Visible Spectrometer instrument (UVVS; Vervack et al. 2010; Sarantos et al. 2011; Burger et al. 2014; Merkel et al. 2017). An example is given in Figure 1. Such observations can be used to constrain our present knowledge on the micrometeoroid vaporization as on the most reliable sources for their generation.

In particular, the present state of understanding of Mercury’s exosphere generated via micrometeoroid impact can be summarized according to the following parameters (both measured and modeled):

1. *Exospheric content.* The observed total calcium exospheric content and its altitude profile can be reproduced in terms of intensity with a model assuming a quenching temperature of the vaporized cloud below 3750 K and considering a two-step process that would initially release CaO, CaOH, and CaOH₂ (Berezhnoy & Klumov 2008; Berezhnoy 2018). The calcium-bearing molecules would be then photodissociated in a second step resulting in the energetic atomic calcium component of the exosphere observed by MESSENGER (see also point 3). Figure 2 shows the modeling results of Moroni et al. (2023) as compared to the MESSENGER observations of Burger et al. (2014).
2. *Altitude profiles.* The equivalent temperatures derived from altitude profiles of neutral calcium and magnesium measurements in the exosphere give values of $\sim 12,000$ – $50,000$ and ~ 6000 K, respectively. These values are consistent with an energetic source process such as micrometeoroid impact vaporization (Killen et al. 2005; Vervack et al. 2010; Burger et al. 2012; Merkel et al. 2017).

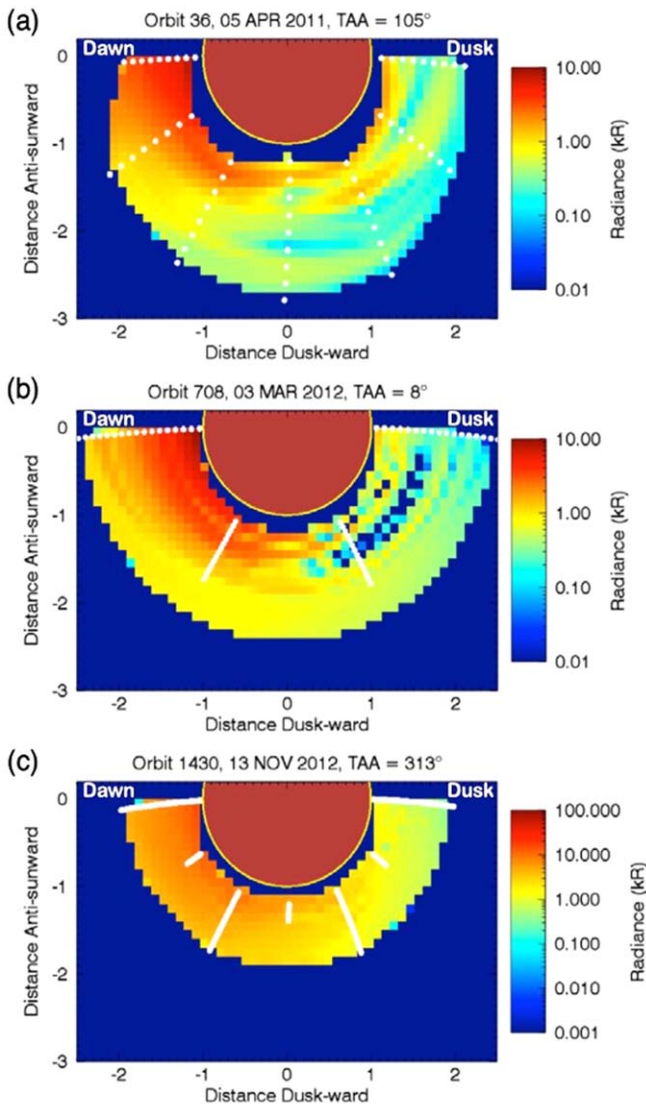


Figure 1. Simulated images of calcium emission in Mercury’s dayside equatorial plane at three different true anomaly angles (TAAs) in Mercury’s orbit. The image was produced by interpolating between UVVS observations where the line of sight crosses the equatorial plane approximately perpendicular (white points; Burger et al. 2014). The color scale indicates the interpolated radiance. Mercury’s sunlit hemisphere is shown. The dawn terminator is to the left and the subsolar point is at the bottom. The white points represent positions where the UVVS line of sight crosses the equatorial plane. The images reflect large-scale local-time variations (small-scale variations in the images are not real). Although the magnitude of the emission varies with Mercury TAA, calcium is always brightest in the dawn hemisphere, usually, but not always, peaking at dawn. From Burger et al. (2014, their Figure 3).

or solar-wind ion sputtering. The best candidate nevertheless is impact vaporization, given that sputtering is expected to be spatially localized mainly in the magnetic cusp regions, while the identified source at the surface for calcium is mainly at dawn at low latitudes (Burger et al. 2014; McClintock et al. 2018).

3. *Different populations.* Even though there is not yet any observational evidence of multi-calcium populations generated via micrometeoroid impact vaporization, Moroni et al. (2023) suggest that two calcium populations at different equivalent temperatures are expected at Mercury (Figure 2): (i) the observed energetic calcium component (temperature about 50,000 K) derived from the shock-

induced nonequilibrium dissociative ionization and neutralization of Ca^+ during the vapor cloud expansion, and (ii) a lower-energy (about 20,000 K) calcium component generated by the photodissociation of the CaO molecules released by micrometeoroid impact vaporization, mostly visible in the post-dawn local times (Figure 2, right panel).

4. *True anomaly angle (TAA).* UVVS observations of the source rate for calcium and magnesium depend on Mercury’s TAA. The observations approximately agree with the variations versus heliocentric distance predicted by Killen & Hahn (2015) and Pokorny (2018). Seasonally, the calcium ultraviolet emission is correlated with the flux of interplanetary dust impacting Mercury’s surface, making these observations consistent with calcium production through impact vaporization (Figure 2). This contrasts with the magnesium production, which shows a much broader peak shortly before perihelion with a minor peak just prior to aphelion (Merkel et al. 2017). Thus, models that adjust dust cloud properties to match the observed calcium seasonal variations cannot fully explain the magnesium observations and vice versa (Johnson & Hauck 2016).
5. *Dawn–dusk asymmetry.* The exospheric magnesium and calcium emissions exhibit pronounced dawn–dusk asymmetries (with the dawn being more intense). This is consistent with the expected asymmetry in the impact vaporization process (McClintock et al. 2009; Burger et al. 2014; Merkel et al. 2017; Pokorny et al. 2017) and, tracing back to the cause, to the leading–trailing asymmetry in the expected flux of meteoroids (Pokorny 2018).
6. *Cometary contribution.* The calcium production peaks shortly after Mercury passes through its perihelion at $\text{TAA} \approx 25^\circ$ (See Section 3.2). This peak likely originates from comet 2P/Encke’s dust trail that intersects Mercury’s orbit at that TAA, leading to dust impacts onto the planet’s surface preferentially near the dawn terminator (Christou et al. 2015; Killen & Hahn 2015). While the distribution profile is well reproduced by simulations, the observed intensities are still much higher than expected (Plainaki et al. 2017) and require further investigation.
7. *Transient events.* MESSENGER observations provide evidence for material being fed into the exosphere via impact vaporization due to meteoroids in the size range of approximately several 10 cm–1 m. In particular, FIPS detected a heavy ion component increase that was interpreted as ion release after a meteoroid impacted Mercury’s surface (Jasinski et al. 2020). In three other events, UVVS detected an exospheric brightness increase by an order of magnitude (Cassidy et al. 2021). In all cases, the hypothesized meteoroids were $\sim 10\text{--}20$ cm in size, with a frequency calculated to be two events per day (Mangano et al. 2007). That study considered meteoritic objects ($1\text{--}10^2$ m) from the Main Asteroid Belt, injected in the inner solar system due to the ν_6 resonances, and predicted clearly visible effects on the most intense components of the exosphere (also on the nightside) that appear now to have been identified.

In summary, the hypervelocity impact of micrometeoroids has now been recognized as a contributing source of refractory elements in Mercury’s exosphere, and recent investigations of MESSENGER data have led to an advancement in our

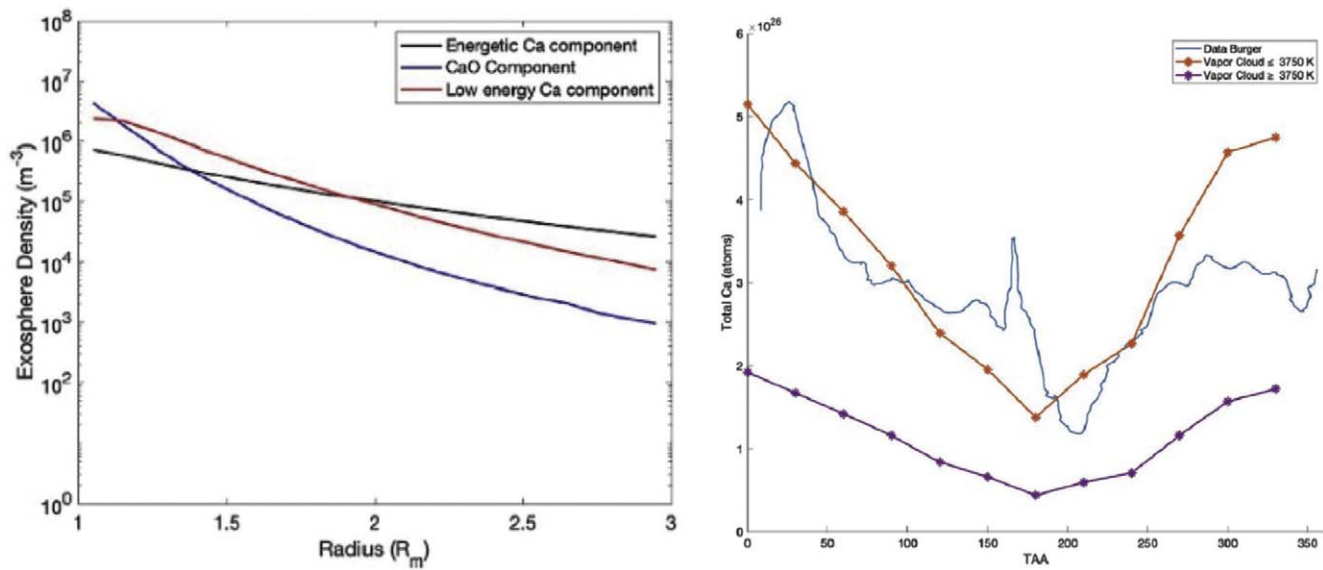


Figure 2. Left: vertical density profiles of the CaO and the calcium components at perihelion (TAA = 0°) assuming a vapor cloud quenching temperature of ≤ 3750 K. Right: comparison between the simulation results obtained in the approximation of the quenching temperature of the vapor cloud ≤ 3750 K (red line) and $=4000$ K (purple line) with the MASCS observations (blue line; Burger et al. 2014) along the Mercury orbit (from Moroni et al. 2023, their Figures 7 and 8).

understanding of the importance of impact vaporization in generating the exosphere. However, there is ongoing debate in the community related to the proportion of the exosphere that may be produced through this mechanism.

For this reason, the future measurements by BepiColombo will be critical for constraining the dust and exospheric environment at Mercury (Benkhoff et al. 2021). In particular, the Mercury Dust Monitor (MDM) on board the Mercury Magnetospheric Orbiter (MMO, or Mio) will be critical to advancing our understanding (Milillo et al. 2020). These measurements will be supported by the complementary instruments on board the Mercury planetary orbiter, including the Search for Exospheric Refilling and Emitted Natural Abundances (SERENA) mass spectrometers and the Probing of Hermean Exosphere By Ultraviolet Spectroscopy (PHEBUS) instrument. These measurements will need to be supported by corresponding advances in laboratory experiments and numerical simulations of hypervelocity impacts, in order to better constrain all the physical parameters necessary for describing the impact and vaporization processes on planetary surfaces.

3. Mercury’s Dust Environment

3.1. Zodiacal Dust Cloud

The flux of hypervelocity impactors on to Mercury’s surface is the result of several different physical processes acting on the source bodies and on the released particles during their passage through interplanetary space. Given its relative accessibility to ground-based and spacecraft-based observations, a wealth of information about dust in the space surrounding the Earth has been obtained to date. The sizes impacting our planet range from (sub)micrometers up to hundreds of meters and even kilometers, thus spanning more than 8 orders of magnitude. Due to the shielding effect of Earth’s atmosphere only the biggest of such objects can hit the surface directly, while the fine dust is decelerated by the atmosphere and gently “rains” down to the surface. These processes are also at work on all other celestial bodies in the solar system; however, the flux,

impactor size distribution, source objects, ejecta yields, and other parameters most likely differ from those near Earth.

The material influx on to, for example, the Moon and Mercury has several effects on the planetary surfaces, including the formation of craters and the well-known effects of impact gardening and space weathering of the soils. However, the significance of the meteoroid impactor flux for Mercury’s exosphere formation compared to other mechanisms is not yet clear (see Section 2). The situation is more complicated in the inner solar system as compared to the environment of the Earth. This is due to the as yet unsettled significance of the various source populations for interplanetary dust, in particular main belt asteroids (MBAs) and comets, although the role of cometary impactors in the inner solar system has become more and more obvious in recent years (Pokorný et al. 2017).

There have been many attempts to model the interplanetary dust environment in the inner solar system. Given that the knowledge of the zodiacal dust cloud beyond Earth orbit is still sparse, the various parameters involved in the problem, e.g., meteoroid mass and velocity distributions and impactor sources, are usually “calibrated” with observations performed at the Earth and at the Moon, and by measurements in the laboratory.

Impacts of asteroidal dust particles have been widely studied as one of the sources of the Hermean exosphere (e.g., Cintala 1992; Marchi et al. 2005; Borin et al. 2009, 2016a), because at the time they were believed to be the dominant source for the meteoroid flux at Earth. Borin et al. (2016a) found that the impactor flux due to asteroidal dust particles should be nonuniform in local time so that only certain regions of Mercury are exposed to dust as a result of the orbital elements of both Mercury and the asteroidal dust particles. The dominance of asteroidal dust has been challenged by Nesvorný et al. (2010, 2011a), who argued that meteoroids in the micrometer to millimeter size range originating from short-period comets (i.e., Jupiter-family comets, JFCs) dominate in the inner solar system in mass flux, number flux, and total cross section. However, this question is far from being settled. For example, recent work has suggested that dust from the Kuiper

Belt is present in significant quantities in the low-velocity part of the dust flux at Mercury (Keller & Flynn 2022).

More recently, Pokorný et al. (2017) demonstrated that the characteristics of the Hermean exosphere is connected with the directionality of the meteoroid influx. Combining dynamical models of dust from JFCs and Halley-type comets (HTCs), the authors demonstrated that the seasonal variation of the meteoroid environment at Mercury, due to the planet's eccentric and inclined orbit, leads to a prominent dawn–dusk exospheric asymmetry as observed by MESSENGER's MASCS/UVVS (Section 2, Figure 1). The location of the highest micrometeoroid influx on to the planet's surface, and thus the region of the strongest impact vaporization, is expected to shift significantly toward the nightside during Mercury's approach to aphelion and toward the dayside when the planet approaches the Sun. The planet's orbital eccentricity and inclination lead to seasonal variations in the impactor flux, impact speed, and impact location.

Furthermore, Pokorný (2018) showed the strong effect of such a dependence on the particle impact speeds. Dust particles originating from MBAs and JFCs impact Mercury preferentially on prograde orbits with low orbital eccentricities $e < 0.2$ and small inclinations $i < 30^\circ$, which results in impact speeds $v_{\text{imp}} < 70 \text{ km s}^{-1}$ at perihelion and $v_{\text{imp}} < 50 \text{ km s}^{-1}$ at aphelion. On the other hand, meteoroids released by HTCs and Oort Cloud comets (OCCs) impact Mercury with a flat eccentricity distribution and a bimodal distribution of orbital inclinations of prograde ($0 < i < 90^\circ$) and retrograde ($90^\circ < i < 180^\circ$) orbits. Retrograde meteoroids predominantly impact Mercury from the planet's direction of motion (apex direction), have impact speeds in the range $95 \text{ km s}^{-1} < v_{\text{imp}} < 120 \text{ km s}^{-1}$ at perihelion and $75 \text{ km s}^{-1} < v_{\text{imp}} < 90 \text{ km s}^{-1}$ at aphelion, and are less influenced by Mercury's orbital motion due to their higher speeds. The high impact speed at Mercury of these dust populations, resulting from retrograde orbits, likely makes them the dominant drivers of physical phenomena affecting the formation and morphology of the planet's exosphere, even though they are likely only a minor part of the meteoroid population in the inner solar system regarding mass flux, number flux, or total meteoroid cross section (Nesvorný et al. 2011b; Pokorný et al. 2014). At Mercury, the mass influx of HTC and OCC dust particles compared to JFC particles could be as small as 5%, but their high impact speeds exceeding 100 km s^{-1} make them the dominant source with respect to impact vaporization or impact yield (Pokorný et al. 2017; Pokorný 2018).

The Pokorný (2018) model shows a strong dawn–dusk asymmetry in the distribution of particle impact directions (radiants; Figure 3). It undergoes significant movement during Mercury's orbit, being centered at the dawn terminator (6 hr local time) at perihelion and aphelion and moving toward the nightside during the outbound leg (maximum displacement of the center is approximately 3 hr) and being shifted toward the dayside in the inbound leg when Mercury moves back to its perihelion. The predicted impact vaporization flux (Figure 4) shows a similar pattern as the source rate for calcium (Burger et al. 2014), i.e., they have a maximum at TAA = 337° and a minimum at 188° , although there are a few exceptions: Enhancements at TAA = 20° , 170° are thought to originate from comet 2P/Encke (Christou et al. 2015; Killen & Hahn 2015 see also Section 3.3). In addition, at $315^\circ \leq \text{TAA} \leq 350^\circ$ the model predicts 30%–40% higher relative

impact vaporization flux than derived from the MESSENGER observations, which remains unexplained.

In addition to the orbital and physical characteristics of the meteoroid influx, the total meteoritic mass impinging onto Mercury is another crucial quantity. Naturally, this is best studied at the Earth, due to the significant amount of data for the Earth/Moon region, which can then be extended to Mercury. However, there is a wide variation of derived fluxes onto Earth, depending on the method used and the connected assumptions and uncertainties, as was illustrated by Plane (2012, their Table 1; see also the review by Janches et al. 2021). Recently, Carrillo-Sanchez et al. (2019) determined a total mass input of $28 \pm 16 \times 10^3 \text{ kg day}^{-1}$ for Earth, with JFC dust being the main contributor, providing about 70% of the total flux. Based on earlier dust flux estimates onto Earth (Carrillo-Sanchez et al. 2016), this leads to the following values of accreted mass averaged over the entire Hermean orbit (Pokorný 2018): MBA dust $M_{\text{MBA}} = 0.26 \pm 0.15 \times 10^3 \text{ kg day}^{-1}$, JFC dust $M_{\text{JFC}} = 7.84 \pm 3.13 \times 10^3 \text{ kg day}^{-1}$, HTC dust $M_{\text{HTC}} = 1.69 \pm 0.91 \times 10^3 \text{ kg day}^{-1}$, and OCC dust $M_{\text{OCC}} = 2.37 \pm 1.38 \times 10^3 \text{ kg day}^{-1}$. These values result in a mass influx ratio of short/long-period comet dust of approximately 2, which is much lower than that at Earth (where it is approximately 7; Carrillo-Sanchez et al. 2016). The vaporization flux averaged over one Mercury orbit then yields $F = 200 \pm 16 \times 10^{-16} \text{ g cm}^{-2} \text{ s}^{-1}$, with a maximum at TAA = 337° of $F_{\text{max}} = 436 \pm 57 \times 10^{-16} \text{ g cm}^{-2} \text{ s}^{-1}$ and minimum at TAA = 188° of $F_{\text{min}} = 82 \pm 12 \times 10^{-16} \text{ g cm}^{-2} \text{ s}^{-1}$ (Pokorný 2018).

It is important to note that the calcium column density in the exosphere of Mercury obtained by Burger et al. (2014) is not linearly proportional to dust mass flux. The calcium delivery rate to the exosphere is a complex function of the quenching temperature of condensation of calcium-containing species, photolysis lifetimes of calcium-containing compounds in the target surface, as well as the initial temperature and pressure in the impact plasma cloud, mass of impacting meteoroids, and the elemental composition of the target and projectile (Berezhnoy et al. 2019).

Finally, the Radio and Plasma Waves (RPW) instrument on board the Solar Orbiter spacecraft detected a dust population with a radial velocity component of approximately 50 km s^{-1} directed outward from the Sun (Zaslavsky et al. 2021). These impactors are likely β meteoroids, i.e., particles driven away from the Sun by solar radiation pressure. The estimated flux at 1 au is roughly $8 \times 10^{-5} \text{ m}^{-2} \text{ s}^{-1}$ for particles with approximately 100 nm radius. This flux and speed are overall consistent with measurements performed with the in situ dust instrument on board the Ulysses spacecraft at 1–3 au heliocentric distance (Wehry et al. 2004). The particles likely originate from mutual collisions of larger particles and by sublimation close to the Sun (Mann 2010). These processes reduce the particle sizes, and once the particles have reached radii as low as approximately 0.1–0.5 μm they become susceptible to the solar radiation force and are accelerated out of the solar system. The significance of these particle impacts onto Mercury's surface for impact vaporization and exosphere formation have not yet been studied.

3.2. Interstellar Dust

In addition to interplanetary dust, which is mostly emitted from comets and asteroids within our solar system

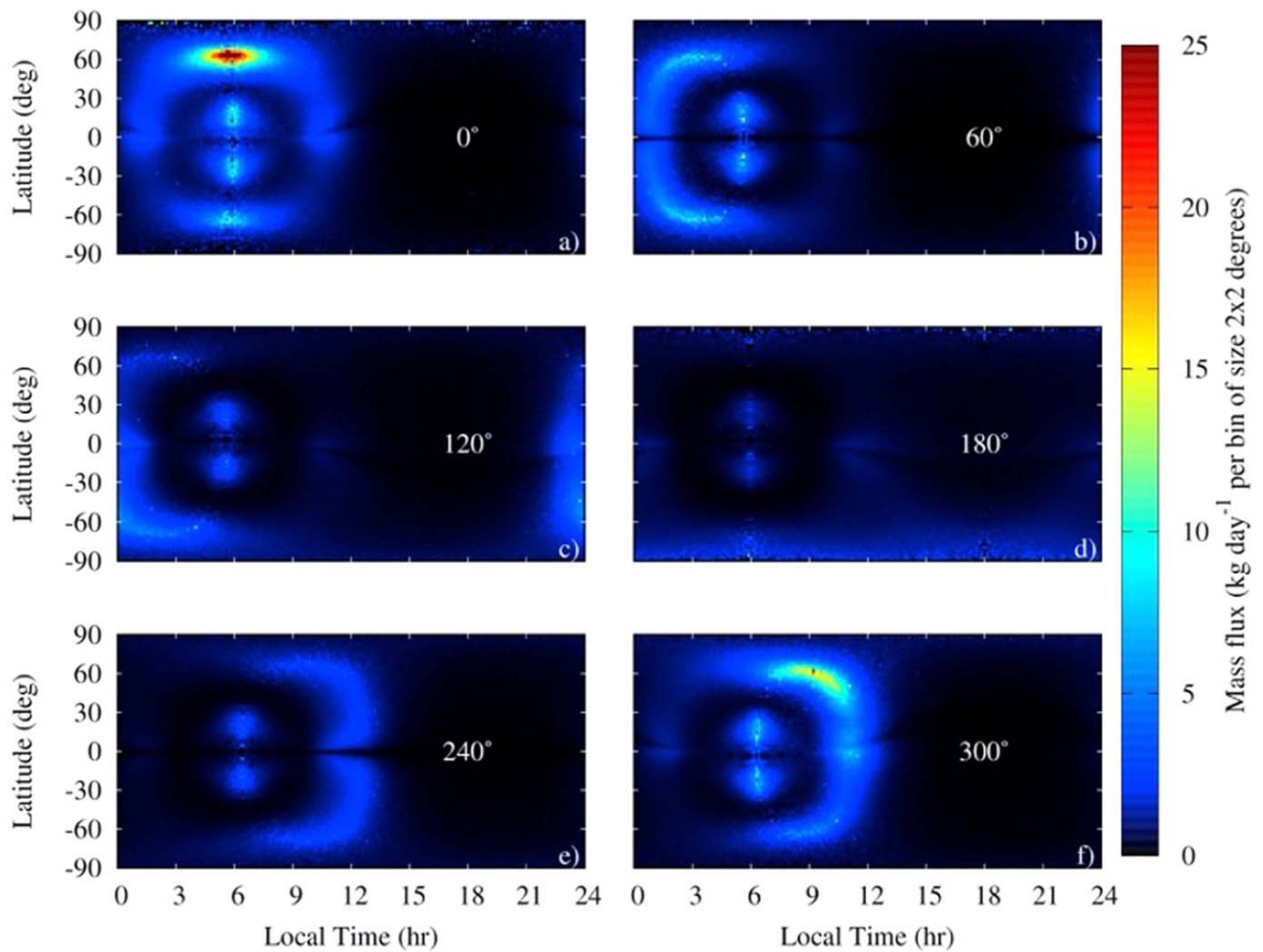


Figure 3. Normalized distribution of meteoroids' approach directions (radiants) impacting Mercury's surface for six different TAAs (Pokorny 2018, their preferred solution). The TAA is given by the white number at 18 hr, 0° in each panel. Mutual meteoroid collisions are not considered. The x -axis represents the local time on Mercury and is fixed with regard to the subsolar point (12 hr). The latitude is measured from Mercury's orbital plane (not the ecliptic plane). From Pokorny et al. (2018, their Figure 24). © AAS. Reproduced with permission.

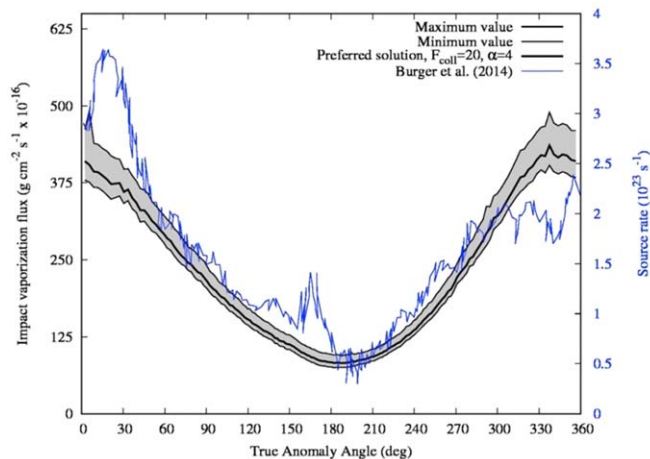


Figure 4. Seasonal variation of the impact vaporization flux from the model of Pokorny (2018, solid thick black line is their preferred solution, see Figure 2, and the confidence interval is marked by the gray area and thin black lines). Also shown are the measurements of exospheric abundance of calcium from Burger et al. (2014, solid blue lines). From Pokorny (2018, their Figure 26). © AAS. Reproduced with permission.

(Section 3.1), there are also interstellar dust particles traversing the heliosphere as the solar system moves through the interstellar medium (Grün et al. 1994; Krüger et al. 2019). These interstellar particles enter the heliosphere from the Sun's apex direction with the velocity of the Sun relative to the Local Interstellar Cloud (26 km s^{-1}). Typically, interstellar dust moves through the solar system on unbound, hyperbolic trajectories. Within the measurement accuracy, the dust inflow direction and speed are the same as those of the neutral interstellar helium gas flow into the solar system (Witte 2004; Lallement & Bertaux 2014; Krüger et al. 2015; Strub et al. 2015; Wood et al. 2015). This is equivalent to the interstellar particles being at rest with respect to the Local Interstellar Cloud.

Kobayashi et al. (2020) performed simulations of interstellar dust with the model by Strub et al. (2019), to predict impact speeds and fluxes of interstellar dust onto Mercury. The model simulates the dynamics of charged micrometer- and submicrometer-sized interstellar particles in the solar system which are exposed to solar gravity, solar radiation pressure, and a time-varying interplanetary magnetic field. The predicted impact

speeds and fluxes of the interstellar particles exhibit strong variations due to the motion of Mercury around the Sun. The impact speeds and fluxes become maximal when Mercury moves opposite to the inflowing interstellar dust stream, and the maximum impact speeds exceed 80 km s^{-1} . Given that the trajectories of the interstellar particles are affected by solar radiation pressure and the solar magnetic field, the impact speeds and fluxes are also modulated by the solar activity (Strub et al. 2019). The effect of interstellar dust impacts onto Mercury's surface for impact vaporization and exosphere formation have not yet been studied.

3.3. Cometary Dust Trails

When a comet becomes active during its orbital motion around the Sun it releases dust particles over a large size range. The smallest submicrometer-sized particles are very quickly blown anti-sunward by the solar radiation pressure, forming the prominent dust tail of a comet. Particles in the intermediate size range from approximately 10 to $100 \mu\text{m}$ are still subject to radiation pressure, thus migrating away from the comet's orbital position, but they can stay on trajectories similar to the orbit of their parent comet for a few revolutions around the Sun. Larger particles with sizes of approximately $100 \mu\text{m}$ to 1 cm are ejected from the cometary nucleus at low speeds and remain very close to the comet orbit for several revolutions around the Sun (Agarwal et al. 2010). They slowly spread in the comet orbit as a result of small differences in orbital period, and form a tubular structure along the orbit of the parent comet filled with dust, called a dust stream or trail.

Cometary dust trails were first observed by the Infrared Astronomical Satellite (Sykes et al. 1986; Sykes & Walker 1992), and in subsequent infrared observations at least 80% of the observed JFCs were associated with dust trails. As a result, dust trails are now considered a generic feature of all comets (Reach et al. 2007). The trails form a fine structure superimposed upon the smooth interplanetary background dust cloud. Unlike the particles in the interplanetary cloud, the trail particles all move on approximately parallel trajectories with nearly the same speed. When the Earth intercepts a cometary trail, the particles collide with the atmosphere and appear as meteors and fireballs with hourly rates significantly enhanced over the sporadic meteor background flux. There have been many attempts to model the dynamical evolution of cometary trails (Jenniskens 2006; Koschny et al. 2019; Janches et al. 2021 and references therein). Effects of meteoroid impacts were also observed on the Earth's Moon and on other planets (Christou et al. 2019). If (micro)meteoroids hit the surface of a celestial body which is not protected by an atmosphere, such as the Moon and Mercury, sufficiently large impacts can become observable as light flashes or detectable in situ as a temporarily enhanced ejecta dust density. These have been reported for the Moon (Szalay & Horanyi 2015a; Horanyi et al. 2015). Such impacts can also temporarily increase the plasma density in the exosphere, as was observed on Mercury (Jasinski et al. 2020).

MESSENGER's MASCS/UVVS observations showed a strong variation of the calcium source rate with TAA (Figure 4). As has been discussed in the previous section, this variation could to a large extent be explained by sporadic micrometeoroid impacts from the interplanetary dust cloud (Killen & Hahn 2015; Pokorny 2018). However, a significant increase in the source rate at $\text{TAA} \sim 25^\circ$ could not be reproduced this way; instead, it was attributed to the

intersection of Mercury's orbit with the dust stream of comet 2P/Encke (Christou et al. 2015; Killen & Hahn 2015). This comet has been linked to several strong daytime and nighttime meteor showers at Earth, the so-called Taurid complex (Whipple 1940; Porubcan et al. 2006). The comet's current orbit is approximately 0.17 au from the Earth orbit but only 0.026 au from that of Mercury (Selsis et al. 2004). This makes it a good candidate for delivering dust to Mercury. Based on observations of Encke's dust trail, the mass loss of the comet was estimated to be approximately 26 kg s^{-1} (Reach et al. 2007), much less than the approximately 1000 kg s^{-1} required to maintain the zodiacal cloud in a steady state (Leinert et al. 1983; Nesvorný et al. 2010). Recently, reflected light from the Encke dust stream near Mercury's orbit was detected in images of the STEREO/Sun Earth Connection Coronal and Heliospheric Investigation instrument (Stenborg et al. 2018).

Christou et al. (2015) modeled the particle dynamics for meteoroids in the dust trail of Encke in order to test the hypothesis that the annually repeatable calcium emission excess in Mercury's exosphere at $\text{TAA} \sim 25^\circ$ is due to the comet's trail particles impacting the planet's surface. Taking solar gravity, planetary perturbations, and Poynting–Robertson drag into account, the simulations showed that millimeter-sized grains ejected 10 – 20 kyr ago encounter Mercury at $\text{TAA} = 350^\circ$ – 30° . Despite the proximity of the orbits of the comet and Mercury, dust released less than 5 kyr ago did not undergo sufficient orbital evolution to reach Mercury. On the other hand, planetary gravitational perturbations begin to disperse the stream after approximately 50 kyr . The position along Mercury's orbit where the excess emission was detected is consistent with a major dust-release episode approximately 20 kyr ago, possibly due to the breakup of Encke's progenitor. The particles released are expected to arrive at Mercury from the antisolar direction and impact on the nightside with impact speeds of 32 – 37 km s^{-1} . The simulations also showed that the stream intersects Mercury's orbit a second time, at $\text{TAA} = 135^\circ$ – 165° , with the meteoroids impacting on the dayside on the outbound leg of their heliocentric trajectories. This is in rough agreement with an enhanced calcium production rate observed at $\text{TAA} \sim 165^\circ$; however, the evidence is less conclusive than for the peak at $\text{TAA} \sim 25^\circ$.

In 2025 December the BepiColombo mission will arrive at Mercury. After orbit insertion, two spacecraft will investigate the planet itself, its exosphere and magnetosphere, and its interaction with the solar-wind plasma. One of the two spacecraft, the magnetospheric orbiter Mio, is equipped with the dust instrument MDM that will be able to detect impacts of approximately micrometer-sized and bigger particles in order to study the dust environment at Mercury (Nogami et al. 2010; Kobayashi et al. 2020). When the planet intercepts Encke's dust trail, and potentially the trails of other comets, detections of trail particles may become possible.

Kobayashi et al. (2020) studied the crossings of cometary dust trails by BepiColombo and Mercury, using a comprehensive dynamical model, the Interplanetary Meteoroid Environment for eXploration Dust Streams in Space model (IMEX; Soja et al. 2015a, 2015b). IMEX follows the evolution of the trails of 420 comets. The model assumes that particles are emitted when a comet is in the inner solar system, and takes comet apparitions between the years 1700 and 2080 into account. Dust ejection is described by an emission model with dust production rates and mass distributions for particle masses

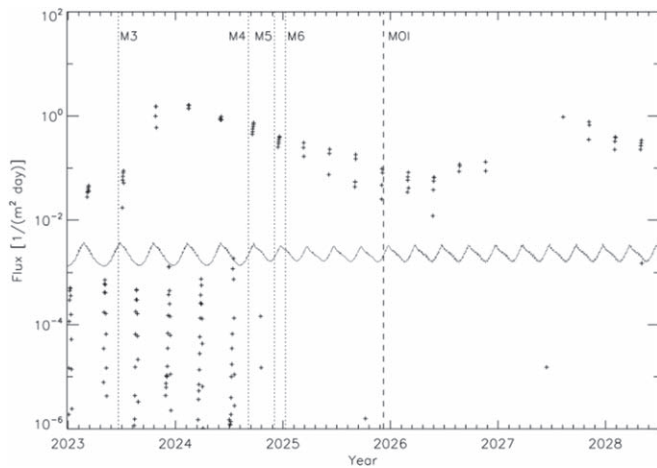


Figure 5. Simulated fluxes of particles larger than $100\ \mu\text{m}$ for crossings of comet 2P/Encke’s dust trail by the BepiColombo spacecraft. The simulations were performed with the Interplanetary Meteoroid Environment for eXploration Dust Streams in Space model (IMEX; Soja et al. 2015a, 2015b) with a 1 day time step. The solid line shows the simulated flux of interplanetary dust particles larger than $100\ \mu\text{m}$, as derived from the Interplanetary Meteoroid Engineering Model (IMEM; Dikarev et al. 2005), for an assumed spherical sensor with a 4π sensor field of view. Vertical dashed lines indicate the Mercury flybys (M3–M6) and Mercury orbit insertion (MOI).

ranging from 10^{-8} kg to 10^{-2} kg (approximately corresponding to $100\ \mu\text{m}$ to 1 cm particles; Soja et al. 2015a). The dust production is calculated from a comet’s absolute magnitude, water production rate, and dust-to-gas ratio. For each emitted particle, the trajectory is integrated under multiple influences, including solar gravity, planetary perturbations, solar radiation pressure, and Poynting–Robertson drag. The model calculates the number density, flux, and impact velocity vector of particles at the spacecraft.

The model results showed that the BepiColombo spacecraft, during its interplanetary cruise to Mercury between 2023 and 2025, will cross the trails of comet Encke and a few other comets (Figure 5). The largest fluxes are predicted for comet Encke’s trail, while for other comets the fluxes are at least 2 orders of magnitude lower (Kobayashi et al. 2020). The crossings of Encke’s trail occur only when the spacecraft ventures within Venus’ orbit after the second Venus flyby in 2022, and the predicted fluxes are the highest in 2024. The flux peaks of these crossings are rather narrow, typically lasting only several days. At Mercury, Encke is the only candidate predicted to produce a significant dust flux, in rough agreement with a dropping number of cometary dust trails in the inner solar system (Jancheš et al. 2021, their Figure 14). The predicted dust fluxes reach up to one impact of a $100\ \mu\text{m}$ or bigger particle per square meter per day. Based on these results, comet Encke is the most promising candidate for detectable trail crossings during the BepiColombo mission.

The IMEX model simulates relatively large particles with radii exceeding $100\ \mu\text{m}$, but cometary trails likely contain smaller particles as well (Agarwal et al. 2010; Krüger et al. 2020). For these smaller particles, their dynamical behavior is not the same as for particles larger than $100\ \mu\text{m}$ due to the increasing effect of nongravitational forces on the smaller particles. However, for radii of $10\text{--}100\ \mu\text{m}$, their orbital characteristics are similar to the larger particles, but spatially offset due to perturbations. The particle sizes follow a cumulative power-law distribution with index of approximately -3 (Agarwal et al. 2010 and references therein). Considering a

lower-mass cutoff at $10\ \mu\text{m}$ and extrapolating the IMEX model flux of $100\ \mu\text{m}$ to bigger particles for a power-law index of -3 leads to an increase in total flux by a factor of 1000. While it is unlikely that all particles in the $10\text{--}100\ \mu\text{m}$ size range remain in the stream, a lower cutoff of $10\ \mu\text{m}$ is still conservative (Krüger et al. 2021, 2024). With the MDM sensitive area of $0.0064\ \text{m}^2$ and detection threshold of $0.5\ \mu\text{m}$ particles (Nogami et al. 2010), a few trail particle impacts should be detectable during each crossing of Encke’s dust trail.

4. Impact-ejecta Dust Clouds

All celestial bodies lacking a gaseous atmosphere are permanently exposed to the bombardment by hypervelocity micrometeoroids which eject dust particles from the surfaces of these bodies, forming regolith and leaving a crater record on the surface. Obviously, all of these bodies should have an ejecta dust cloud.

Measurements of impact ejecta in space can give more insight into the process of hypervelocity dust ejection, linking the effects observed for the surface with the impactor meteoroid flux, for which laboratory experiments on Earth have not yet revealed a comprehensive understanding. They can be treated as a natural impact experiment in an astrophysically relevant environment, extending laboratory measurements in two important ways: (i) the projectile and target materials are astrophysically relevant, and (ii) the masses and speeds of the ejecta particles can be determined in a region of parameter space not easily accessible to experiments (i.e., micrometer sizes and kilometer-per-second impact speeds).

4.1. Dust Cloud Measurements

Until the 1990s there were only a few attempts at in situ detections of impact ejecta close to satellites—most notably, near the Earth’s Moon (Iglesider et al. 1996). These experiments, however, did not lead to definitive results. At Jupiter, the in situ dust detector on board the Galileo spacecraft successfully measured ejecta of hypervelocity impacts in the vicinities of source moons for the first time. All four Galilean moons were shown to possess impact-ejecta dust clouds (Krüger et al. 1999, 2000, 2003). These measurements stimulated the development of numerical models for such clouds (Krivov et al. 2003; Sremcevic et al. 2003; Szalay & Horanyi 2015a; Szalay et al. 2018). The vast majority of ejecta particles are released from the surface with initial speeds below the escape speed from the target moons ($\approx 2\ \text{km s}^{-1}$). Thus, assuming that nongravitational forces are negligible, the dust particles follow ballistic trajectories and eventually fall back to the surface, blanketing the surface with a highly pulverized regolith. Limited by the small number of particle detections at the time, the models mostly considered the case of a spherically symmetric cloud, and an attempt to model asymmetries in the clouds due to particle impact speeds and impactor fluxes varying with local time and latitude was not supported by the Galileo measurements due to the small number of detections (Sremcevic et al. 2003). Nevertheless, due to the lack of measurements at the Moon since the 1960s and 1970s, the measurements at Jupiter stimulated progress in the exploration of the lunar dust environment.

In this regard, the Lunar Atmosphere and Dust Environment Explorer (LADEE) mission (Elphic & Russell 2015) provided the next major step forward in understanding impact-ejecta dust

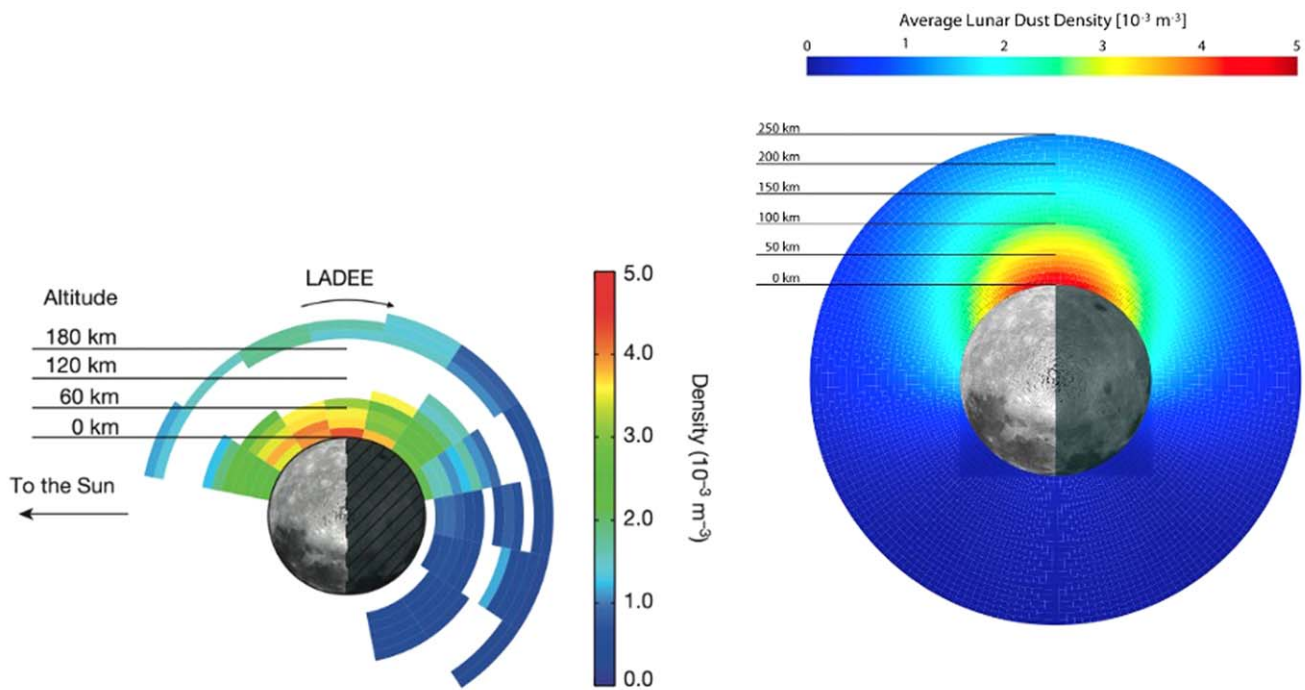


Figure 6. Lunar dust density distribution in a reference frame where the Sun is in the $-x$ direction and the apex motion of the Moon about the Sun is in the $+y$ direction. Left: top-down view of the dust density for particles with $s > 0.3 \mu\text{m}$. LDEX did not make measurements between 12 and 18 hr local time, while it was pointed near the direction of the motion of the spacecraft. The white coloring indicates regions where LADEE did not visit or was not set up for normal operations. From Horanyi et al. (2015, their Figure 3). Right: modeled annually averaged lunar dust density distribution for particles with $s > 0.3 \mu\text{m}$. From Szalay & Horanyi (2016a, their Figure 3).

clouds. LADEE was designed to directly measure the ejecta cloud generated by meteoroid impacts onto the Moon. During its 7 month orbital mission at the Moon, the Lunar Dust EXperiment (LDEX) on board LADEE successfully measured lunar dust down to altitudes of approximately 25 km, as shown in Figure 6 (Horanyi et al. 2015). LDEX was an impact-ionization dust detector similar to the dust instruments on board the Galileo and Ulysses spacecraft (Grün et al. 1992a, 1992b) which measured impacts of dust particles larger than approximately $0.3 \mu\text{m}$ (Horanyi et al. 2014). The instrument provided crucial measurements to improve existing models for the interplanetary dust environment at 1 au (Szalay & Horanyi 2015a), and led to better constraints for the overall connection between meteoroid bombardment and exosphere formation. LDEX detected a total of approximately 140,000 dust impacts during almost 3 months of cumulative operation time. Unlike the Galilean moons, an exponential fit was found to be in good agreement with the altitude distribution of dust in the lunar impact-ejecta cloud (Szalay & Horanyi 2016a). Reviews of the LDEX results were given by Szalay et al. (2018) and Janches et al. (2021).

The LDEX measurements showed that the Moon is immersed in a permanent, but highly variable ejecta dust cloud. The cloud is asymmetric, with a density maximum at 6–8 hr lunar local time, i.e., in the ram direction of the orbital motion of the Earth–Moon system about the Sun, with the peak density being shifted somewhat sunward of the dawn terminator (Figure 6). The cloud density is modulated by both the Moon’s orbital motion around the Earth and the Earth’s motion around the Sun. Impacts of particles released from long-period comets (i.e., HTC and OCC) play a major role in the production of the observed ejecta cloud (Szalay & Horanyi 2015a). The cloud is primarily produced by impacts

from a combination of the three known sporadic meteoroid sources (Helion, Anti-Helion, and Apex). The lunar ejecta dust gets dispersed through the Earth–Moon system (Yang et al. 2022).

Analogous to the ejecta clouds observed at the Galilean moons and the Earth’s Moon, impact ejecta should be generated from airless bodies throughout the solar system. For example, Szalay et al. (2018, 2019) applied their model, originally developed for the lunar dust cloud, to predict dust clouds surrounding asteroids, including (3200) Phaethon, which is the target of the upcoming DESTINY⁺ mission (Arai et al. 2018). Mercury likely possesses an impact-ejecta cloud similar to the Moon but probably denser given the higher meteoroid flux deeper in the heliosphere (Hahn et al. 2002; Müller et al. 2002; Pokorny et al. 2017), although the overall magnitude of the meteoroid flux at Mercury is still fairly uncertain (Borin et al. 2016b; Borin 2016c; Pokorny 2018).

Recent studies have shown that the asymmetric distribution of impactors onto Mercury’s surface causes significant variations in the impacting dust flux with Hermean local time and latitude (Borin et al. 2016a; Pokorny 2018). Impacts from comet Encke’s dust trail are held responsible for transient increases in exospheric plasma densities when Mercury crosses this trail (Section 3.3). However, despite these findings, no comprehensive model for the Hermean impact-ejecta dust cloud has been developed to date. Only Müller et al. (2002), stimulated by the Galileo measurements at Jupiter and the BepiColombo mission being on the horizon at the time, modeled the spatial density of impact-ejecta particles around Mercury, assuming possible Hermean surface conditions. They found a model uncertainty of almost 4 orders of magnitude due to the poorly constrained surface material and model parameters. In other words, precise estimation of the physical

properties of impact ejecta are challenging because they depend upon still poorly constrained surface conditions, such as material strength, grain size, grain shape, and porosity (Housen & Holsapple 2011). Future in situ measurements of the impact-ejecta cloud in the vicinity of Mercury with MDM on board BepiColombo/Mio (Nogami et al. 2010) will help better constrain the planet’s impact-ejecta dust cloud and the conditions for impact ejection in general.

4.2. A Model for an Impact-generated Dust Cloud

The development of a model for particle dynamics in impact-ejecta dust clouds was motivated by the Galileo measurements at Jupiter in order to test the hypothesis of the impact ejection mechanism and to estimate the mass budgets in the clouds. Several model parameters had to be adopted from laboratory impact experiments. Here we only sketch the basic procedure for developing such a model, with special emphasis for Mercury as the target. For more details, the reader is referred to Krivov & Hamilton (1997), Müller et al. (2002), Krivov et al. (2003), Szalay & Horanyi (2015a), and Szalay et al. (2018).

The model can be developed in two steps. First, the production rate of dust from the surface of the parent body is considered. This requires a number of parameters. The mass flux of interplanetary impactors can be estimated from the model of, for example, Nesvorný et al. (2011a) and Pokorný (2018). It is dominated by grains with masses $m \sim 10^{-8}$ kg (corresponding to particle radii of approximately 100 μm ; Grün et al. 1985; Nesvorný et al. 2011a). Because of the randomly distributed inclinations, the velocities relative to Mercury of the fastest particles, i.e., particles originating from HTCs and OCCs, exceed 100 km s^{-1} (Section 3.1), with a typical average of approximately 50 km s^{-1} . Corrections are necessary for gravitational focusing by Mercury. This increases the interplanetary dust flux, F , by a factor of $1 + (v_{\text{esc}}/v_d)^2$, where v_d is the velocity of the dust particle at a large distance from the planet and v_{esc} is the escape speed from the planet’s surface (Dohnanyi 1978). However, given that $v_{\text{esc}} \ll v_d$ and the large uncertainties of some of the parameters involved, gravitational focusing can be neglected to a first approximation.

Second, the production of impact ejecta is considered. The efficiency of ejection in a cratering event is characterized by the characteristic yield, Y , which is defined as the ratio of the ejected mass to the projectile mass. Typical yields for hypervelocity impacts derived from laboratory experiments range from $\sim 10^3$ to 10^6 (Lange & Ahrens 1987). A typical value for 10^{-8} kg impactors and impact speeds of $v \sim 25 \text{ km s}^{-1}$ gives characteristic yields of $Y \approx 10^4$ (e.g., Koschny & Grün 2001a; Szalay et al. 2018 and references therein). The mass production rate from the body’s surface is then calculated as $M^+ = FYS$, with $S = \pi R^2$ being the cross-sectional area of the body hit by the impactors and R the radius of the body. A typical assumption is that the ejecta fragments are distributed in a cone with a half-opening angle ranging from 0° to 90° with a given angular distribution (see, e.g., Horanyi et al. 2015).

The cumulative mass distribution of the ejecta is described by a power law $N^+(\gt m) \propto m^{-\alpha}$, where m is the grain mass and $N^+(\gt m)$ the number of particles with masses greater than m ejected from the target body per second. The ejecta mass and speed distributions were obtained from impact experiments (Koschny & Grün 2001b) and are consistent with the Galileo and LADEE data (Szalay et al. 2018). To calculate the total amount of ejecta material, the mass distribution requires an

assumption about the mass of the heaviest ejecta fragment. A reasonable assumption for the maximum ejecta mass is $m_{\text{max}} = 10^{-8}$ kg, which is close to the typical mass of impactors (the results depend only weakly on this parameter). In order to predict ejecta dust densities and fluxes measurable with a dust instrument, the (speed-dependent) detection threshold has to be taken into account, and the mass distribution has to be calculated for particles above this threshold.

Once the ejecta production rate $N^+(\gt m)$ is calculated, the second step is to model the steady-state distribution of dust surrounding the target body. The initial speed u distribution of the ejecta is taken as a power law $\Psi(\gt u) = (u/u_0)^{-\gamma}$, where $u \geq u_0$ (e.g., Stöffler et al. 1975; Hartmann 1985). Here $\Psi(\gt u)$ is the fraction of the material ejected at speeds exceeding u . The parameters u_0 and γ depend on the target material and mass, as well as the speed and mass of the projectiles. Both have to be determined from impact experiments. Typically, the lower cutoff values of the ejecta speed u_0 are tens of meters per second. The distribution slope γ ranges from about 1 for loose, regolith-like targets to about 2 for harder surfaces such as low-temperature ice (e.g., Frisch 1992; Colwell & Esposito 1993). Any correlations between the speeds of the ejected grains and their masses at the moment of ejection may be ignored because laboratory experiments still do not imply strong relationships between both quantities (Nakamura & Fujiwara 1991), although impact experiments for bigger particles (Nakamura et al. 1994) and theoretical modeling (Melosh 1984) suggest that larger fragments are on average launched with lower speeds. Sachse et al. (2015) dropped the assumption that the ejecta sizes and ejection speeds are uncorrelated and applied their new model to dust clouds around planetary satellites. They find that both the uncorrelated and correlated models can fit in situ measurements of the total density equally well, but differences are visible for micron-sized or larger particles, implying that the exact form of the correlation is poorly constrained (see also Section 8).

Two separate populations of ejecta particles can be considered: particles moving on ballistic trajectories which fall back to their target surface shortly after ejection, and those fast enough to escape from the gravity field of the parent body. For micrometer-sized and bigger dust, which is not significantly affected by nongravitational forces, the ejecta can be assumed to move on Keplerian trajectories—pieces of ellipses and hyperbolas, respectively, which can be considered as an excellent approximation. Finally, possible effects of nonisotropy of the impactor flux or temporal variations have to be considered (e.g., Colwell 1993; Sremcevic et al. 2003; Szalay & Horanyi 2016b, 2020).

Under these assumptions, exact solutions for the number densities of dust, both on ballistic and unbound trajectories can be derived (Krivov et al. 2003). To a first approximation, the number density of dust grains ejected into ballistic trajectories, which dominates the cloud at distances below several radii of the parent body, is given by $n_{\text{bound}}(x) \propto x^{-5/2}$, where $x \equiv r/R_{\text{obj}}$ is the distance r measured in radii of the parent body, R_{obj} . The equation shows that the number density decreases with increasing distance from the parent body. The drop of the number density is steeper than 2 because larger distances can be reached only by particles ejected at higher speeds, which are less abundant than slower ejecta. The radial number density profile only weakly depends on the angular distribution of the ejecta. The contribution of unbound grains escaping into the

cloud is somewhat shallower, i.e., $n_{\text{unbound}}(x) \propto x^{-2}$, which slightly flattens the overall radial profile at larger distances from the parent body, closer to its Hill radius.

The parameters chosen were compatible with the Galileo data at the time, supporting the conclusion about the impact origin of the detected grains. Any improvement of the poorly known parameters (yield, slope of the ejecta speed distribution, etc.) was not possible because of the scarcity of the small number of detected particles. Even with the better LADEE data, it was not possible to remove the dependencies between some model parameters (Szalay et al. 2018).

5. Electrostatically Lofted Dust

In addition to micrometer-sized and bigger impacts which eject dust from airless bodies, there has been evidence for electrostatic processes contributing to the evolution and transport of fine dust on, for example, the Moon and asteroids. Images taken by the Surveyor spacecraft from the lunar surface just after sunset and just before sunrise showed a horizon glow which was interpreted as forward-scattered sunlight from a cloud of dust particles levitated less than 1 m above the surface with particle radii of approximately $5 \mu\text{m}$ (Rennilson & Criswell 1974). However, theoretical investigations implied that strong cohesive forces cause the preferential sizes for particle launching to be orders of magnitude larger than the approximately $0.1\text{--}5 \mu\text{m}$ particles commonly considered (Hartzell & Scheeres 2011; Masiero et al. 2021). This is supported by experimental work, which showed that larger aggregates of dust particles are more likely to exhibit motion than individual submicrometer particles. Thus, cohesion is likely a significant force affecting the launching process, and the mechanism through which charged dust particles are launched off the surface of an airless body is currently poorly understood. In particular, no mechanism capable of generating sufficiently large electric fields or dust grain charges to levitate micrometer-sized particles has been identified (Hartzell & Scheeres 2011).

One of the experiments deployed by the Apollo 17 mission on the lunar surface was the Lunar Ejecta and Meteorites (LEAM) experiment. It registered a multitude of unexpected hits during lunar sunrise and sunset (Berg et al. 1976). A recent reanalysis by Grün & Horanyi (2013) of part of the data set still available suggests that these signals were not caused by slow-moving and highly charged dust grains transported across the lunar surface, but instead were related to noise in the data.

High-altitude observations performed by the Apollo missions from lunar orbit indicated the existence of lofted dust at tens of kilometers altitude above the surface (McCoy & Criswell 1974; McCoy 1976). Some of these images indicated an excess brightness interpreted as forward-scattered light from small grains with characteristic radii of approximately $0.1 \mu\text{m}$ lofted over the terminator regions of the Moon by electrostatic effects. Upper limits on the dust densities derived from Clementine remote-sensing observations (Glenar et al. 2014) and from in situ measurements performed by LADEE/LDEX (Szalay & Horanyi 2015b) were up to 4 orders of magnitude lower than the values originally derived (McCoy 1976; Glenar et al. 2011). Thus, neither the Clementine observations nor the LADEE in situ measurements provided evidence for the existence of electrostatically lofted grains at high altitudes above the lunar terminators. This leads us to conclude that the major mechanism for the formation of the lunar dust cloud must be impact-ejecta formation (Section 4).

Features on asteroid (433) Eros that morphologically resemble ponds may indicate that electrostatic levitation and transport is a significant process on asteroidal surfaces (Veverka et al. 2001; Hughes et al. 2008). Laboratory measurements of dust in a plasma sheath show that dust launched off the surface by electrostatic levitation can indeed provide a sufficient source for transport to produce the observed Eros ponds (Colwell et al. 2005). Observations of Saturn's small moon Atlas have also suggested that electrostatic transport processes may occur (Hirata & Miyamoto 2012), and Jupiter's strong magnetic field may be sufficient for lofting of micrometer- and submicrometer-sized dust grains from the surfaces of the inner Jovian moons Amalthea and Thebe (Borisov & Krüger 2020). However, a competing theory suggests boulder erosion could lead to similar phenomena (Dombard et al. 2010). Finally, electrostatic lofting of dust particles with the aid of mobile alkali ions at high temperatures may be responsible for the activity of (3200) Phaethon (Masiero et al. 2021; Kimura et al. 2022; MacLennan & Granvik 2024).

For airless bodies with relatively low gravity, electrostatic transport may play a role in the transport and depletion of surface dust. Recent laboratory studies have shown that dust exposed to ultraviolet light and/or incident plasma indeed experiences small-scale transport (Colwell et al. 2007; Wang et al. 2016). The latter reference proposed a “patched surface charge” model to explain how individual micrometer- and submicrometer-sized dust grains may attain sufficient electric charge, thus allowing significant electrostatic acceleration of grains on to ballistic trajectories above a charged surface. With regard to the question whether dust can be lifted or not, cohesion, i.e., mutual particle sticking and particles sticking to the surface, is likely a key player dictating the dynamics of electrostatically lofted dust (Hartzell & Scheeres 2011; Hartzell et al. 2013; Kimura et al. 2014). For example, Hirata et al. (2022) suggested that the formation of the spokes in the Saturnian rings, which has previously been attributed to electrostatic processes, may be due to temperature-dependent cohesion. Lunar and asteroidal observations as well as laboratory experiments have all suggested that small-scale electrostatic mobilization and transport occurs on airless bodies throughout the solar system. However, many open questions remain, and this phenomenon represents an active field of research (Szalay et al. 2018).

6. Nature of Target Materials and Surface Effects

The surface environment at Mercury is unlike any other planetary body in the inner solar system. The MESSENGER mission revealed that Mercury's composition is enigmatic. Direct measurements of the surface abundances of many key rock-forming elements were performed with the X-Ray Spectrometer instrument. These results revealed the widespread presence of moderately volatile elements, notably Na, K, and S (up to 4 wt.%; Nittler et al. 2011; Peplowski et al. 2011), extremely low Fe abundance (<2 wt.%; Nittler et al. 2011; Evans et al. 2012; Weider et al. 2014), and the presence of a darkening agent widespread across the surface, likely graphitic C (Murchie et al. 2015; Peplowski et al. 2015). Models suggest this graphite is remnant of a primary flotation crust in the planet's early history (Murchie et al. 2015; Vander Kaaden & McCubbin 2015; Peplowski et al. 2016; Klima et al. 2018). These chemical signatures point toward a planet that formed

under highly reduced conditions and which hosts a volatile-rich mineralogy. Combining compositional with geomorphological data enabled the description of distinct geological units in addition to possible mineralogies (Peplowski et al. 2015; Weider et al. 2015; Vander Kaaden et al. 2017).

Multispectral imaging by the Mercury Dual Imaging System wide-angle camera on MESSENGER showed that Mercury's surface contains widespread, smooth volcanic plains (Denevi et al. 2009; Head et al. 2011). In general, these plains have high reflectance and red spectral slopes, although this geological unit can be further subdivided based on geographic location, with regions at high polar latitudes being dubbed Borealis Planitia (BP). Another major formation, corresponding to the darkest materials on the surface, is the low-reflectance material (LRM), which is spatially correlated with the floors and rims of impact craters and basins. The darkening agent in the LRM is thought to be a C-bearing phase, primarily graphite (Klima et al. 2018). The geochemistry of these units, which includes C-rich LRM and low-Fe, high-S BP units, presents an entirely new compositional regime, for which space weathering and the effects of micrometeoroid bombardment may cause diverging effects compared to other well-studied inner solar system bodies. The diverse geological units on Mercury may lead to an ejected dust population and vapor plumes generated by impacts that have compositions reflective of the unique surface compositions (e.g., impacts have been proposed as a cause of Mg species in the exosphere; see Section 2 and Sarantos et al. 2011). In addition to the ejection of material from the surface and generation of components of Mercury's exosphere, dust impacts on the surface have also been proposed to generate distinct microstructural and chemical characteristics in the regolith (as is discussed in the next section).

7. Expected Effects on Surface Materials

7.1. The Role of Dust in Space Weathering at Mercury

The fundamental drivers of surface alteration on airless bodies are impact-related processes, thermal processing, and irradiation. Here we primarily consider the effects of impacts. The flux of impactors at airless body surfaces results in gardening and comminution, turning bedrock into poorly consolidated regolith at scales ranging from submicrometer to many kilometers. Much of our knowledge regarding these processes comes from studies of the lunar surface through remote-sensing and returned sample analyses. For the lunar case (and presumably for the Hermean case as well) it is the larger impactors (>centimeter) that drive gardening, e.g., the excavation and burial of regolith materials. This contrasts with the higher-flux millimeter-sized impactors and smaller micrometeoroids, which generate an active surface layer extending only a few centimeters in depth where regolith particles are impacted and reworked, referred to as the reworking zone (Gault et al. 1974). Subsequent work has shown that secondary impacts of ejecta generated during primary impact events drive much of the surface reworking in the upper few centimeters, by ~ 2 orders of magnitude, compared to primary impacts (Speyerer et al. 2016; Costello et al. 2018), resulting in a near surface that behaves in a similar manner to a fluidized bed, constantly cycling grains from the surface through the reworking zone. The flux of >centimeter impactors at Mercury is lower than at the Moon, although velocities are higher, with a mean velocity of $\sim 30 \text{ km s}^{-1}$, ranging up to 80 km s^{-1}

(Marchi et al. 2005), resulting in a lower regolith reworking depth on Mercury than the Moon (Costello et al. 2020). In contrast to the centimeter-scale reworking depth, the gardening rate by micrometeoroids in the uppermost few millimeters on Mercury is not well constrained.

To better constrain the impactor flux for particles <centimeter and to investigate the production rates of impact-generated melting and vaporization and erosion of volatiles on Mercury relative to the Moon and Ceres, the community has turned to numerical methods. Modeling efforts have demonstrated that the impactor flux for particles <centimeter is ~ 5.5 times greater at Mercury than that at the Moon, that Mercury has a $50\times$ higher mass flux than Ceres, and that the mode of impact velocities are also $\sim 50\%$ higher at Mercury (15.8 km s^{-1} versus 9.8 km s^{-1}), with maximum velocities $40\text{--}60 \text{ km s}^{-1}$ (Cintala 1992; Borin et al. 2009; Pokorný et al. 2021). These differences in impact velocity and total flux largely determine the relative production rates of melt and vapor in the respective regoliths, resulting in ~ 15 times more melt and ~ 20 times more vapor produced per unit area and unit time on Mercury compared to the Moon (Cintala 1992). Higher impact velocities also suggest that the relative proportion of vapor to melt generated during these dust impacts is significantly higher at Mercury than for bodies around 1 au. With this in mind, predictions suggest that there are few surviving crystalline grains expected in the Mercurian regolith (Cintala 1992).

7.2. Predicted Microstructural and Chemical Products of Space Weathering on Mercury

Armed with information regarding the impact velocities and fluxes at Mercury, we can explore the potential microstructural and chemical products resulting from hypervelocity impacts through the lens of lunar samples. The major impact-produced materials in lunar regolith are the characteristic agglutinates (glass-welded aggregates formed through micrometeoroid impacts into fine-grained regolith particles), melt splashes and impact spherules, and surface coatings formed by the condensation of impact-generated vapors (Figure 7; Keller & McKay 1993, 1997). These impact processes drive the evolution of regoliths from immature, to submature, and finally to mature status, with such designations based on grain size and agglutinate content (e.g., McKay et al. 1974). Mature lunar soils achieve a relatively steady state between comminution of soil particles and agglutinate formation in $\sim 10^7$ yr (McKay et al. 1974). Recent work to understand the outermost ~ 100 nm of grain surfaces (space-weathered rims) of individual soil particles from mature soils show that they develop typically after a few million years of surface exposure (Keller et al. 2021). Opaque nano- and microphase particles are common in the impact-produced materials in the lunar regolith and have major effects on optical properties. The dominant opaque in lunar materials is Fe metal particles as inclusions in melt glass and in grain coatings. The sizes of Fe metal grains vary and impart different effects in terms of spectral characteristics (Figure 7). It is the smaller ($\sim <40$ nm) Fe metal inclusions that result in spectral "reddening" in optical reflectance spectra over visible wavelengths, whereas the larger Fe metal grains result in darkening (e.g., Keller et al. 1998; Noble et al. 2007). More recent studies have identified additional opaque components in lunar samples including Fe silicides (e.g., Hapkeite and associated phases; Anand et al. 2004) and phases that likely

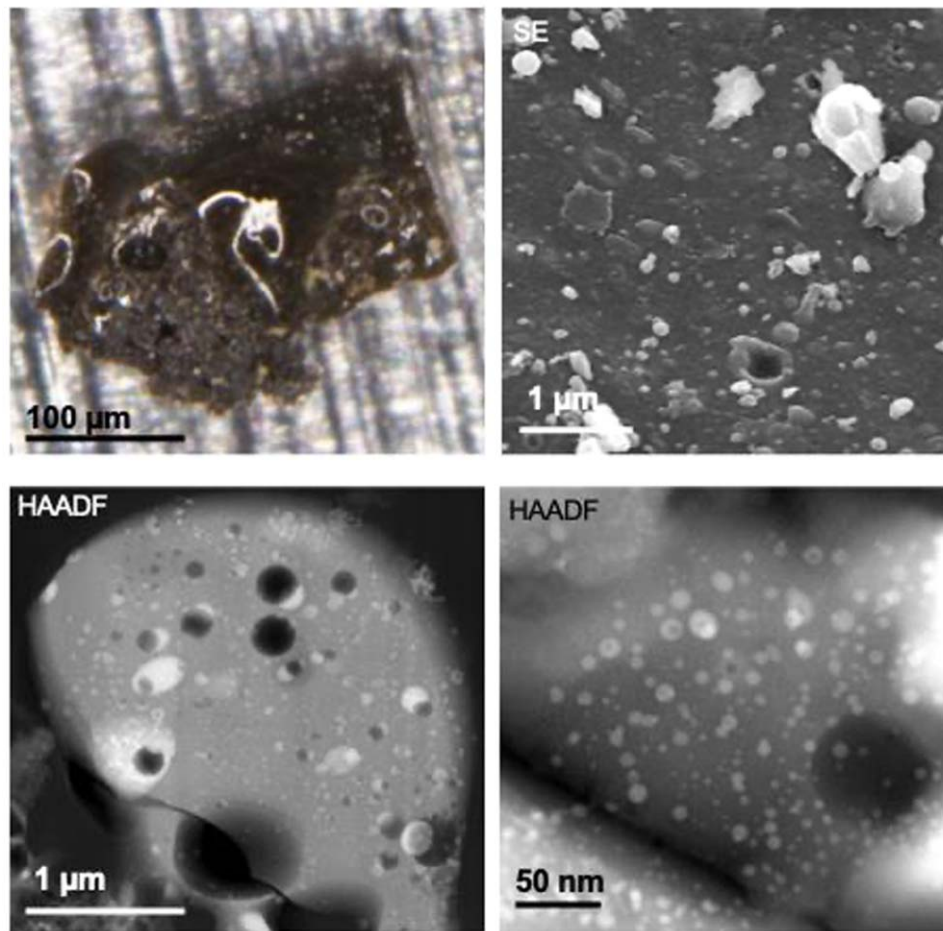


Figure 7. Top left: impact products including visible-light image of a lunar agglutinate from Apollo 11 soil sample with shiny glass coating and vesicles on the surface. Top right: secondary electron (SE) image of the surface of a lunar rock showing evidence of micrometeoroid impacts including microcraters, melt spherules, melt splashes, etc. Bottom left and right: cross-section images of regolith grains from Ryugu in high-angle annular dark field (HAADF) imaging and Apollo 17, respectively, in a transmission electron microscope. Bright spherules of nanophase Fe-bearing particles, ranging in size from a few nanometers to hundreds of nanometers in diameter, can be seen in the images.

form through oxidation processes by reaction with surrounding glass and/or H_2O , including FeO and Fe_3O_4 (e.g., Thompson et al. 2016; Burgess & Stroud 2018). In returned samples from S-type and C-type asteroids, we observe nanoparticles enriched in S, including FeS , MgS (Noguchi et al. 2011, 2014, 2023), and FeNiS . When we consider the composition of opaque phases beyond the Moon, the microstructural characteristics produced via space weathering are predicted to be heavily dependent on the starting composition of the surface. These observations suggest that nanophase products on Mercury may have unique compositions compared to other airless bodies, particularly when considering the low-Fe, S-rich surface composition. Predictions for the mineralogy of nanophase inclusions on Mercury include FeS , MgS , possible Fe silicides, and polymorphs of carbon including amorphous carbon and graphite (McCubbin et al. 2017; Trang et al. 2017, 2018). In addition, nanophase particles that are able to form in impact glasses are predicted to be larger than those from lunar samples because of an Ostwald ripening process resulting from higher surface temperature on Mercury (Noble & Pieters 2003; Trang et al. 2017; Deutsch et al. 2022).

For the lunar case, the width of grain rims that form via the deposition of impact-generated vapors are not correlated with exposure time (as measured using solar flare track exposure ages). This is in contrast to predictions of the gradual

accumulation of the amorphous rims with time. Instead, the deposition is believed to be episodic with the bulk of material condensing in a few events on the Moon (Keller et al. 2021). We expect that the vapor deposits on Mercurian regolith grains will be thicker and better correlated with exposure age compared to lunar rims because of the higher impactor flux and velocities at Mercury.

7.3. Laboratory Experiments Simulating Micrometeoroid Impacts at Mercury

In the absence of returned samples or landed missions, we have to explore impact space-weathering processes in the laboratory to better understand the development of microstructural and chemical features that might form in the surface regolith at Mercury. To experimentally simulate micrometeoroid impacts, we can perform pulsed-laser irradiation under vacuum. This technique was adopted to simulate the short-duration, high-temperature effects associated with the extreme energy transfers characteristic of hypervelocity impacts (Moroz et al. 1996; Yamada et al. 1999; Sasaki et al. 2001; Hiroi et al. 2004; Loeffler et al. 2016; Thompson et al. 2019, 2020, 2021). This technique has been shown to accurately recreate the spectral effects of space weathering in mafic minerals (e.g., reddening, darkening, and attenuation of absorption bands in

the visible–near-infrared wavelengths). Subsequent analyses using transmission electron microscopy confirmed the production of melt and vapor deposits containing nanophase Fe particles that resemble those observed in returned samples from the Moon (Sasaki et al. 2001, 2003). Furthermore, electron microscopy studies have shown that spectral characteristics correlate to the nature and concentration of the nanophase Fe in these deposits (Brunetto et al. 2006; Loeffler et al. 2008, 2016).

To date, there have been limited space-weathering studies that investigate the effects of simulated micrometeoroid impacts on materials that are compositionally analogous to Mercury’s surface. Sasaki & Kurahashi (2004) performed pulsed-laser simulations of olivine (8.97% wt.% FeO) and pyroxene (9.88 wt.% FeO) and showed that the spectra of these samples were redder and darker after irradiation. However, these experiments did not target samples with <4 wt.% in FeO, or samples with S- and/or C-rich phases, all of which are expected to be present on the Mercurian surface. In addition, Trang et al. (2018) performed pulsed-laser irradiation of materials with a range of compositions, some of which were more appropriate Hermean analogs. These experiments used analog samples with compositions including quartz mixed with graphite in varying proportions, and pure graphite. The results of these experiments revealed a reddening and darkening of the reflectance spectra of the quartz-graphite mixtures. Spectral modeling pointed toward the likely presence of submicroscopic carbon particles in glassy silicate rims in the quartz-graphite mixtures. After laser irradiation experiments on silicate regolith with various FeO contents (Moroz et al. 2014), more recent work by Bott et al. (2023) focused on laser irradiation experiments of experimentally synthesized olivine samples with FeO content ranging from 0.1 wt.% to 1.0 wt.% mixed with 5 wt.% graphite to represent the C-rich regions of the LRM. For these studies, Si wafers were suspended above the samples to collect vapor and melt ejected from the surface of the sample during the simulated impact. These experiments have shown progressive reddening of the visible–near-infrared reflectance spectra with progressive irradiation (e.g., increased total number of laser pulses). Electron microscopy analyses have revealed unique microstructural and chemical characteristics, including micron-thick amorphous melt layers depleted in Mg with embedded C-rich nanoparticles and highly vesiculated graphite grains (Bott et al. 2023). Furthermore, particles and vapor deposited on the Si wafer after irradiation include MgO, suggesting there is evidence for an impact source of Mg in the exosphere (Sarantos et al. 2011). These experiments have demonstrated that space weathering on Mercury might result in both familiar and new structural and chemical characteristics. The impact that these characteristics have on the interpretation of remote-sensing data for Mercury collected by MESSENGER and, eventually, BepiColombo, is still not well understood.

8. Outlook and Next Steps

Detailed below, the next major steps forward for understanding the dust environment at Mercury should include the following:

1. Analysis of the Hermean dust environment using the MDM instrument on board BepiColombo, including comparison to existing models.
2. Provide constraints on impact-generated dust cloud models via laboratory experiments and measurements.

3. Improved models to understand grain lofting and lifetimes in the regolith.
4. Laboratory experiments to better understand the chemical, microstructural, and spectral effects of micrometeoroid impacts on the surface.
5. Link these results to MESSENGER and upcoming BepiColombo data.

The BepiColombo mission, which will arrive at the planet in 2025 December, will provide a wealth of new data about the Mercury dust environment. The mission will place two spacecraft in close orbits around Mercury to study the planet’s interior, surface, exosphere, and magnetosphere during several Mercury years. One of the two spacecraft, the MMO (or Mio; Benkhoff et al. 2021), carries the MDM, which is dedicated to study dust in the Hermean environment (Nogami et al. 2010; Kobayashi et al. 2020). MDM is a dust impact detector that will directly measure dust particle impacts in Mercury’s region of the solar system (0.31–0.47 au), measuring their impact momentum and approximate impact direction with a field of view covering almost a half sphere. The MDM system is composed of a 64 cm² piezoelectric PZT sensor unit (MDM-S) attached to the outside of Mio’s side panel, and an electronics unit (MDM-E) installed behind the panel. The PZT sensor adopted by MDM can tolerate high temperatures (about +1700°C). MDM is also capable of detecting dust particles arriving from the solar direction. Given that Mio is a spin-stabilized spacecraft, MDM can detect dust particles from all directions during one spin-revolution of the spacecraft.

At Mercury’s location in the solar system, we expect to detect β -meteoroids which are on solar-radiation-pressure-driven escape trajectories from the solar system. Such particles are expected to arrive from the approximate direction of the Sun. In addition, interplanetary dust will be detectable which moves on Keplerian orbits. The Helios spacecraft performed in situ dust measurements in the spatial region of Mercury, but MDM will accumulate micrometeoroid data with less noise using a high-temperature-tolerant sensor. Micrometeoroid bombardment may be one of the significant contributors to the formation process of Mercury’s tenuous exosphere (Section 2). Comparison of the micrometeoroid data with exospheric observations of Mercury’s environment will help to solve the mystery of its formation process. β -meteoroids and interplanetary dust particles bombard Mercury’s surface and launch impact-ejecta particles to high altitudes. The bombardment of micrometeoroids continuously occurs on airless bodies, and the impact-ejecta particles form a so-called “dust cloud” surrounding the body (Section 4). The same is expected to occur on Mercury. When cometary dust trails, like that of comet Encke, intersect Mercury’s orbit, the spatial number density of dust cloud particles around Mercury is also expected to increase (Section 3.3). Observational data of the dust cloud particles may provide evidence in this regard, revealing a relationship with variations in Mercury’s exosphere. To interpret the upcoming MDM measurements in terms of the interplanetary dust impactor environment, models are readily available (Pokorny 2018), including ESA’s Interplanetary Meteoroid Engineering Model 2 (IMEM2; Soja et al. 2019) and the IMEX Dust Streams in Space model (Soja et al. 2015a, 2015b).

There is no comprehensive model available for the Hermean dust cloud created by the impact-ejecta mechanism. Only the earlier model by Müller et al. (2002) exists up to now. The

parameters involved in the dust cloud modeling have been summarized in Section 4.2. These include the impact-ejecta yields, ejecta size, speed and directional distributions, projectile speeds and impact angle, among others. All these parameters are only poorly constrained by existing laboratory measurements, and more experiments are needed in this field. Housen & Holsapple (2011) recently reviewed the state of knowledge. Material properties like composition (e.g., minerals, water ice), strength, density, porosity, etc. play an important role, and studies of the impact-ejecta process over a large parameter range are needed. For example, various authors obtained quite different maximum ejection speeds from the craters formed upon impact, ranging from approximately $700\text{--}800\text{ m s}^{-1}$ up to 20 km s^{-1} .

There also remain significant outstanding questions regarding how dust impacts affect regolith development and cycling on the Mercurian surface, and how dust moves across the surface. Many of these topics can be tackled via improved modeling efforts. One priority should include the exploration of grain lifetimes with respect to micrometeoroid impactor flux (Section 7.2). Similarly, better modeling efforts to understand the conditions under which dust may be lofted across the surface would be timely. In addition, refining Mercurian regolith processing models (Cintala 1992) with updated constraints from current and improved lunar impact gardening models (Costello et al. 2020), along with new insights into the dust environment at Mercury (Pokorný & Kucher 2019), would improve our understanding of how regolith is cycled on the surface. Furthermore, we must explore the outstanding unknowns and incorporate the results to provide more accurate models for the role of dust impacts on Mercurian regolith.

In addition to modeling efforts, laboratory experiments will be critical for understanding the effects of dust impacts on the chemical, microstructural, and spectral characteristics of Mercurian regolith (Section 7.3). To ensure the applicability of our experiments, we must evaluate the best methodologies for simulating micrometeoroid impacts in the laboratory. While pulsed-laser irradiation has become our most commonly employed technique, dust accelerators and in situ heating experiments in an electron microscope have both been employed to explore these processes; and we should examine their efficacy in relation to Mercury. The analysis of returned samples from the Moon and near-Earth asteroids has demonstrated that micrometeoroid impacts produce complex changes in surface regolith (Section 7.2). The accumulation of these nanoscale features has a significant effect on the spectral properties of the surface that are observed with remote-sensing spacecraft. Findings from existing laboratory studies highlight how critical it is to investigate fully the role that composition, which is uniquely volatile-rich and Fe-poor for Mercury compared to other inner solar system bodies, plays in space weathering via micrometeoroid impacts (Section 7.1). With the diverse nature of potential geological units on Mercury, we must examine the full compositional spectrum in order to understand surface processing more broadly across the planet. Similarly, experiments may provide constraints for the possibility of impacts producing mineralogically diverse optically active phases, as the microstructural products have a largely unknown influence on the spectral characteristics of the Mercurian surface. To understand the effects of these nanophases, we must prioritize laboratory measurements of optical properties of nanophase and microphase silicides, sulfides, and other species across various size regimes (nanometer to micrometer). The community must

undertake coordinated spectral and sample-based studies to understand how dust impacts alter the regolith at Mercury and provide guidance for targeted BepiColombo measurements that would be relevant to these knowledge gaps. Together, these analyses would significantly improve our ability to interpret results from MESSENGER and the upcoming BepiColombo mission and would greatly expand our knowledge of the role dust plays in forming the exosphere and in modifying the surface of Mercury.










Acknowledgments

The IMEM and IMEM2 models and the IMEX Dust Streams in Space model were developed under ESA funding (contracts 21928/08/NL/AT, 4000114513/15/NL/HK, and 4000106316/12/NL/AF - IMEX). M.T. appreciates support from NASA SSW grant No. 80NSSC23K0560. L.K. was supported in part by the Johnson Space Center Coordinated Analysis Work Package funded by the NASA Internal Scientist Funding Model. D.D. and D.W.S. were supported, in part, by the NASA solar system Workings grant Nos. 80NSCC18K0521 and 80NSCC22K0099. A.G. acknowledges support by the Swiss National Science Foundation (grant No. 200021L_182771/1).

Appendix

Acronyms	
DESTINY+	Demonstration and Experiment of Space Technology for Interplanetary voYage Phaethon fLyby and dUst Science spacecraft
ESA	European Space Agency
FIPS	Fast Imaging Plasma Spectrometer on board MESSENGER spacecraft
IMEM	Interplanetary Meteoroid Engineering Model
IMEX	Interplanetary Meteoroid Environment for eXploration dust streams in space model
JAXA	Japanese Aerospace Exploration Agency
JFC	Jupiter-family comet
HTC	Halley-type comet
LADEE	Lunar Atmosphere and Dust Environment Explorer spacecraft
LDEX	Lunar Dust EXperiment on board LADEE spacecraft
LEAM	Lunar Ejecta and Meteorites experiment
LRM	Low-reflectance material
MASCS	Mercury Atmosphere and Surface Composition Spectrometer on board MESSENGER spacecraft
MBA	Main belt asteroid
MDM	Mercury Dust Monitor instrument on board BepiColombo spacecraft
MESSENGER	MErcury Surface, Space ENvironment, GEOchemistry, and Ranging spacecraft
MMO	Mercury Magnetospheric Orbiter spacecraft of the BepiColombo mission, also called Mio
OCC	Oort Cloud Comet
PHEBUS	Probing of Hermean Exosphere By Ultraviolet Spectroscopy instrument on board BepiColombo spacecraft
RPW	Radio and Plasma Waves instrument on board Solar Orbiter spacecraft
SECCI	Sun Earth Connection Coronal and Heliospheric Investigation instrument on board STEREO spacecraft
SERENA	Search for Exospheric Refilling and Emitted Natural Abundances instrument on board BepiColombo spacecraft
STEREO	Solar TERrestrial RELations Observatory spacecraft
TAA	True anomaly angle
UVVS	UltraViolet and Visible Spectrometer on board MESSENGER spacecraft

ORCID iDs

Michelle S. Thompson  <https://orcid.org/0000-0003-0824-9225>
 Valeria Mangano  <https://orcid.org/0000-0002-9903-4053>
 Anna Milillo  <https://orcid.org/0000-0002-0266-2556>
 Lindsay P. Keller  <https://orcid.org/0000-0003-1560-2939>
 Deborah Domingue  <https://orcid.org/0000-0002-7594-4634>
 André Galli  <https://orcid.org/0000-0003-2425-3793>
 François LeBlanc  <https://orcid.org/0000-0002-5548-3519>
 Menelaos Sarantos  <https://orcid.org/0000-0003-0728-2971>
 Daniel W. Savin  <https://orcid.org/0000-0002-1111-6610>

References

- Agarwal, J., Müller, M., Reach, W. T., et al. 2010, *Icar*, 207, 992
 Altobelli, N., Grün, E., & Landgraf, M. 2006, *A&A*, 448, 243
 Anand, M., Taylor, L. A., & Nazarov, M. A. 2004, *PNAS*, 101, 6847
 Andrews, G. B., Zurbuchen, T. H., Mauk, B. H., et al. 2007, *SSRv*, 131, 523
 Arai, T., Kobayashi, M., Ishibashi, K., et al. 2018, *LPSC*, 49, 2570
 Berezhnoy, A. A. 2018, *Icar*, 300, 210
 Benkhoff, J., Murakami, G., Baumjohann, W., et al. 2021, *SSRv*, 217, 90
 Benkhoff, J., van Casteren, J., Hayakawa, H., et al. 2010, *P&SS*, 58, 2
 Berezhnoy, A. A., & Klumov, B. A. 2008, *Icar*, 195, 511
 Berezhnoy, A. A., Velikodsky, Y. I., Zubko, E., et al. 2019, *P&SS*, 177, 104689
 Berg, O. E., Wolf, H., & Rhee, J. 1976, in *IAU Colloq. 31, Interplanetary Dust and Zodiacal Light*, ed. H. Elsaesser & H. Fechtig (Cambridge: Cambridge Univ. Press), 233
 Bernardoni, E., Horanyi, M., Doner, A., et al. 2022, *PSJ*, 3, 69
 Borin, P. 2016c, *A&A*, 588, C3
 Borin, P., Cremonese, G., Bruno, M., & Marzari, F. 2016a, *Icar*, 264, 220
 Borin, P., Cremonese, G., & Marzari, F. 2016b, *A&A*, 585, A106
 Borin, P., Cremonese, G., Marzari, F., Bruno, M., & Marchi, S. 2009, *A&A*, 503, 259
 Borisov, N., & Krüger, H. 2020, *P&SS*, 183, 104556
 Bott, N., Thompson, M. S., Vander Kaaden, K. E., Loeffler, M. J., & McCubbin, F. M. 2023, *LPSC*, 54, 1696
 Brunetto, R., Romano, F., Blanco, A., et al. 2006a, *Icar*, 180, 546
 Burger, M. H., Killen, R. M., McClintock, W. E., et al. 2012, *JGRE*, 117, E00L11
 Burger, M. H., Killen, R. M., McClintock, W. E., et al. 2014, *Icar*, 238, 51
 Burgess, K. D., & Stroud, R. M. 2018, *JGRE*, 123, 2022
 Carrillo-Sanchez, J. D., Gomez-Martín, J. C., Bones, D. L., et al. 2019, *Icar*, 335, 113395
 Carrillo-Sanchez, J. D., Nesvorný, D., Pokorný, P., Janches, D., & Plane, J. M. C. 2016, *GeoRL*, 43, 11,979
 Cassidy, T. A., Schmidt, C. A., Merkel, A. W., Jasinski, J. M., & Burger, M. H. 2021, *PSJ*, 2, 175
 Christou, A., Vaubaillon, J., Withers, P., Hueso, R., & Killen, R. 2019, in *Meteoroids: Sources of Meteors on Earth and Beyond*, ed. G. O. Ryabova et al. (Cambridge: Cambridge Univ. Press), 119
 Christou, A. A., Killen, R. M., & Burger, M. H. 2015, *GeoRL*, 42, 7311
 Cintala, M. J. 1992, *JGR*, 97, 947
 Colwell, J. 1993, *Icar*, 106, 536
 Colwell, J. E., & Esposito, L. W. 1993, *JGR*, 98, 7387
 Colwell, J. E., Gulbis, A. A. S., Horanyi, M., & Robertson, S. 2005, *Icar*, 175, 159
 Colwell, J. E., Horanyi, M., Robertson, S., et al. 2007, in *ESA SP-643, Workshop on Dust in Planetary Systems*, ed. H. Krueger & A. Graps (Houston, TX: LPI), 171
 Costello, E. S., Ghent, R. R., Hirabayashi, M., & Lucey, P. G. 2020, *JGRE*, 125, e06172
 Costello, E. S., Ghent, R. R., & Lucey, P. G. 2018, *Icar*, 314, 327
 Denevi, B. W., Robinson, M. S., Solomon, S. C., et al. 2009, *Sci*, 324, 613
 Dermott, S. F., Gogan, K., & Durda, D. D. 2001, in *Interplanetary Dust*, ed. E. Grün et al. (Berlin: Springer), 569
 Deutsch, A., Neumann, G. A., Trang, D., Izenberg, N., & Denevi, B. W. 2022, *Mercury 2022*, ed. F. Leblanc et al. (Paris: CNRS), 72
 Dikarev, V., Grün, E., Baggaley, J., et al. 2005, *AdSpR*, 35, 1282
 Dohnanyi, J. S. 1978, in *Cosmic Dust*, ed. J. A. M. McDonnell (Chichester: Wiley), 527
 Dombard, A. J., Barnouin, O. S., Prockter, L. M., & Thomas, P. C. 2010, *Icar*, 210, 713
 Domingue, D. L., Chapman, C. R., Killen, R. M., et al. 2014, *SSRv*, 181, 121
 Elphic, R. C., & Russell, C. T. 2015, *The Lunar Atmosphere and Dust Environment Explorer Mission (LADEE)* (Cham: Springer)
 Evans, L. G., Peplowski, P. N., Rhodes, E. A., et al. 2012, *JGRE*, 117, E00L07
 Fechtig, H., Leinert, C., & Berg, O. E. 2001, in *Interplanetary Dust*, ed. E. Grün et al. (Berlin: Springer), 1
 Flandes, A., Krüger, H., Hamilton, D. P., et al. 2011, *P&SS*, 59, 1455
 Frisch, W. 1992, in *Proc. of the Workshop on Hypervelocity Impacts in Space*, ed. J. A. M. McDonnell (Canterbury: Univ. Kent), 7
 Gault, D. E., Hörz, F., Brownlee, D. E., & Hartung, J. B. 1974, *LPSC*, 5, 2365
 Giberson, W. E., & Cunningham, N. W. 1975, *AcAau*, 2, 715
 Glenar, D. A., Stubbs, T. J., Hahn, J. M., & Wang, Y. 2014, *JGRE*, 119, 2548
 Glenar, D. A., Stubbs, T. J., McCoy, J. E., & Vondrak, R. R. 2011, *P&SS*, 59, 1695
 Grava, C., Killen, R. M., Benna, M., et al. 2021, *SSRv*, 217, 61
 Grün, E., Fechtig, H., Hanner, M. S., et al. 1992a, *SSRv*, 60, 317
 Grün, E., Fechtig, H., Kissel, J., et al. 1992b, *A&AS*, 92, 411
 Grün, E., Gustafson, B. E., Mann, I., et al. 1994, *A&A*, 286, 915
 Grün, E., & Horanyi, M. 2013, *P&SS*, 89, 2
 Grün, E., Krüger, H., & Srama, R. 2019, *SSRv*, 215, 46
 Grün, E., Pailer, N., Fechtig, H., & Kissel, J. 1980, *P&SS*, 28, 333
 Grün, E., Zook, H. A., Fechtig, H., & Giese, R. 1985, *Icar*, 62, 244
 Gurnett, D. A., Grün, E., Gallagher, D., Kurth, W. S., & Scarf, F. L. 1983, *Icar*, 53, 236
 Hahn, J. M., Zook, H. A., Cooper, B., & Sunkara, B. 2002, *Icar*, 158, 360
 Hartmann, W. K. 1985, *Icar*, 63, 69
 Hartzell, C. M., & Scheeres, D. J. 2011, *P&SS*, 59, 1758
 Hartzell, C. M., Wang, X., Scheeres, D. J., & Horányi, M. 2013, *GeoRL*, 40, 1038
 Head, J. W., Chapman, C. R., & Strom, R. G. 2011, *Sci*, 333, 1853
 Hirata, N., Kimura, H., & Ohtsuki, K. 2022, *Icar*, 378, 114920
 Hirata, N., & Miyamoto, H. 2012, *Icar*, 220, 106
 Hiroi, T., Pieters, C. M., Rutherford, M. J., et al. 2004, *LPSC*, 35, 1616
 Horanyi, M. 1996, *ARA&A*, 34, 383
 Horanyi, M., Sternovsky, Z., Lankton, M., et al. 2014, *SSRv*, 185, 93
 Horanyi, M., Szalay, J. R., Kempf, S., et al. 2015, *Natur*, 522, 324
 Housen, K. R., & Holsapple, K. A. 2011, *Icar*, 211, 856
 Howard, R. A., Vourlidas, A., Bothmer, V., et al. 2019, *Natur*, 576, 232
 Hsu, H.-W., Krüger, H., & Postberg, F. 2012, in *Nanodust in the Solar System: Discoveries and Interpretations (Astrophysics and Space Science Library, Vol. 385)* ed. I. Mann, N. Meyer-Vernet, & A. Czechowski (Heidelberg: Springer), 77
 Hsu, H.-W., Postberg, F., Sekine, Y., et al. 2015, *Natur*, 519, 207
 Hughes, A. L. H., Colwell, J. E., & Dewolfe, A. W. 2008, *Icar*, 195, 630
 Hughes, A. M., Duchene, G., & Matthews, B. C. 2018, *ARA&A*, 56, 541
 Iglseider, H., Uesugi, K., & Svedhem, H. 1996, *AdSpR*, 17, 177
 Janches, D., Berezhnoy, A. A., Christou, A. A., et al. 2021, *SSRv*, 217, 50
 Jasinski, J. M., Regoli, L. H., Cassidy, T. A., et al. 2020, *NatCo*, 11, 4350
 Jenniskens, P. 2006, *Meteor Showers and their Parent Comets* (Cambridge: Cambridge Univ. Press)
 Johnson, C. L., & Hauck, S. A. 2016, *JGRE*, 121, 2349
 Jones, M. H. 2017, *Icar*, 288, 172
 Jones, M. H., Bewsher, D., & Brown, D. S. 2013, *Sci*, 342, 960
 Jonker, G., van Elsland, R., van der Lubbe, J. H. J. L., & van Westrenen, W. 2023, *M&PS*, 58, 463
 Kameda, S., Kagitani, M., & Okano, S. 2011, *LPSC*, 42, 1608
 Kameda, S., Yoshikawa, I., Kagitani, M., & Okano, S. 2009, *GeoRL*, 36, L15201
 Keller, L. P., Berger, E. L., Zhang, S., & Christoffersen, R. 2021, *M&PS*, 56, 1685
 Keller, L. P., & Flynn, G. J. 2022, *NatAs*, 6, 731
 Keller, L. P., & McKay, D. S. 1993, *Sci*, 261, 1305
 Keller, L. P., & McKay, D. S. 1997, *GeCoA*, 61, 2331
 Keller, L. P., Wentworth, S. J., & McKay, D. S. 1998, *LPSC*, 29, 1762
 Kempf, S. 2018, *EPSC*, EPSC2018-462
 Khawaja, N., Postberg, F., Hillier, J., et al. 2019, *MNRAS*, 489, 5231
 Killen, R., Bida, T., & Morgan, T. 2005, *Icar*, 173, 300
 Killen, R. M., Burger, M. H., Vervack, R. J., & Cassidy, T. A. 2018, in *Mercury: The View after MESSENGER*, ed. S. C. Solomon, L. R. Nittler, & B. J. Anderson (Cambridge: Cambridge Univ. Press), 407
 Killen, R. M., & Hahn, J. M. 2015, *Icar*, 250, 230
 Kimura, H., & Mann, I. 1999, in *Meteoroids 1998*, ed. W. J. Baggaley & V. Porubcan (Bratislava: Astronomical Inst., Slovak Academy of Sciences), 283
 Kimura, H., Ohtsuka, K., Kikuchi, S., et al. 2022, *Icar*, 382, 115022
 Kimura, H., Senshu, H., & Wada, K. 2014, *P&SS*, 100, 64
 Klima, R. L., Denevi, B. W., Ernst, C. M., Murchie, S. L., & Peplowski, P. N. 2018, *GeoRL*, 45, 2945
 Kobayashi, M., Shibata, H., Nogami, K., et al. 2020, *SSRv*, 216, 144
 Kobayashi, M., Srama, R., Krüger, H., Arai, T., & Kimura, H. 2018, *LPSC*, 49, 2050
 Koschny, D., & Grün, E. 2001a, *Icar*, 154, 391
 Koschny, D., & Grün, E. 2001b, *Icar*, 154, 402
 Koschny, D., Soja, R. H., Engrand, C., et al. 2019, *SSRv*, 215, 34

- Krivov, A. V., & Hamilton, D. P. 1997, *Icar*, **128**, 335
- Krivov, A. V., Sremcevic, M., Spahn, F., Dikarev, V. V., & Kholshchikov, K. V. 2003, *P&SS*, **51**, 251
- Krüger, H., Horanyi, M., Krivov, A. V., & Graps, A. L. 2004, in *Jupiter. The Planet, Satellites and Magnetosphere*, Vol. 1, ed. B. Fran, T. E. Dowling, & W. B. McKinnon (Cambridge, UK: Cambridge Univ. Press), 219
- Krüger, H., Kobayashi, M., Strub, P., et al. 2021, *EP&S*, **73**, 93
- Krüger, H., Krivov, A. V., & Grün, E. 2000, *P&SS*, **48**, 1457
- Krüger, H., Krivov, A. V., Hamilton, D. P., & Grün, E. 1999, *Natur*, **399**, 558
- Krüger, H., Krivov, A. V., Sremcevic, M., & Grün, E. 2003, *Icar*, **164**, 170
- Krüger, H., Strub, P., Altobelli, N., et al. 2019, *A&A*, **626**, A37
- Krüger, H., Strub, P., Sommer, M., et al. 2020, *A&A*, **643**, A96
- Krüger, H., Strub, P., & Grün, E. 2024, *RSPTA*, submitted
- Krüger, H., Strub, P., Sterken, V. J., & Grün, E. 2015, *ApJ*, **812**, 139
- Lallement, R., & Bertaux, J. L. 2014, *A&A*, **565**, A41
- Lange, M. A., & Ahrens, T. J. 1987, *Icar*, **69**, 506
- Larsen, J., & Genge, M. J. 2016, 79th Annual Meeting of the Meteoritical Society, 6341
- Leinert, C., & Moster, B. 2007, *A&A*, **472**, 335
- Leinert, C., Roser, S., & Buitrago, J. 1983, *A&A*, **118**, 345
- Loeffler, M. J., Baragiola, R. A., & Murayama, M. 2008, *Icar*, **196**, 285
- Loeffler, M. J., Dukes, C. A., Christoffersen, R., & Baragiola, R. A. 2016, *M&PS*, **51**, 261
- Malaspina, D. M., Stenborg, G., Mehoke, D., et al. 2022, *ApJ*, **925**, 27
- MacLennan, E., & Granvik, M. 2024, *NatAs*, **8**, 60
- Mangano, V., Milillo, A., Mura, A., et al. 2007, *P&SS*, **55**, 1541
- Mann, I. 2010, *ARA&A*, **48**, 173
- Mann, I., & Czechowski, A. 2021, *A&A*, **650**, A29
- Mann, I., Kimura, H., Biesecker, D. A., et al. 2004, *SSRv*, **110**, 269
- Marchi, S., Morbidelli, A., & Cremonese, G. 2005, *A&A*, **431**, 1123
- Masiero, J. R., Davidsson, B. J. R., Liu, Y., Moore, K., & Tuite, M. 2021, *PSJ*, **2**, 165
- McClintock, W. E., Cassidy, T. A., Merkel, A. W., et al. 2018, in *Mercury: The View after MESSENGER*, ed. S. C. Solomon, L. R. Nittler, & B. J. Anderson (Cambridge: Cambridge Univ. Press), 371
- McClintock, W. E., Vervack, R. J., Bradley, T., et al. 2009, *Sci*, **324**, 610
- McCoy, J. E. 1976, *LPSC*, **7**, 1087
- McCoy, J. E., & Criswell, D. R. 1974, *LPSC*, **5**, 2991
- McCubbin, F. M., Vander Kaaden, K. E., Peplowski, P. N., et al. 2017, *JGRE*, **122**, 2053
- McKay, D. S., Fruland, R. M., & Heiken, G. H. 1974, *LPSC*, **5**, 887
- Melosh, H. J. 1984, *Icar*, **59**, 234
- Merkel, A. W., Cassidy, T. A., Vervack, R. J., et al. 2017, *Icar*, **281**, 46
- Meyer-Vernet, N., Maksimovic, M., Czechowski, A., et al. 2009, *SoPh*, **256**, 463
- Milillo, A., Fujimoto, M., & Murakami, G. 2020, *SSRv*, **216**, 1
- Milillo, A., Wurz, P., Orsini, S., et al. 2005, *SSRv*, **117**, 397
- Moroni, M., Mura, A., & Milillo, A. 2023, *Icar*, **401**, 115616
- Moroz, L. V., Fisenko, A. V., Semjonova, L. F., Pieters, C. M., & Korotaeva, N. N. 1996, *Icar*, **122**, 366
- Moroz, L. V., Starukhina, L. V., & Rout, S. S. 2014, *Icar*, **235**, 187
- Mukai, T., Yamamoto, T., Hasegawa, H., Fujiwara, A., & Koike, C. 1974, *PASJ*, **26**, 445
- Müller, M., Green, S. F., McBride, N., et al. 2002, *P&SS*, **50**, 1101
- Murchie, S. L., Klima, R. L., Deveni, B. W., et al. 2015, *Icar*, **254**, 287
- Nakamura, A., & Fujiwara, A. 1991, *Icar*, **92**, 132
- Nakamura, A. M., Fujiwara, A., & Kadono, T. 1994, *P&SS*, **42**, 1043
- Nesvorný, D., Janches, D., Vokrouhlický, D., et al. 2011a, *ApJ*, **743**, 129
- Nesvorný, D., Vokrouhlický, D., Pokorný, P., & Janches, D. 2011b, *ApJ*, **743**, 37
- Nesvorný, D., Jenniskens, P., Levison, H. F., et al. 2010, *ApJ*, **713**, 816
- Nittler, L. R., Starr, R. D., Weider, S. Z., et al. 2011, *Sci*, **333**, 1847
- Noble, S. K., & Pieters, C. M. 2003, *SoSyR*, **37**, 34
- Noble, S. K., Pieters, C. M., & Keller, L. P. 2007, *Icar*, **192**, 629
- Nogami, K., Fujii, M., Ohashi, H., et al. 2010, *P&SS*, **58**, 108
- Noguchi, T., Kimura, M., Hashimoto, T., et al. 2014, *M&PS*, **49**, 188
- Noguchi, T., Matsumoto, T., Miyake, A., et al. 2023, *NatAs*, **7**, 170
- Noguchi, T., Nakamura, T., Kimura, M., et al. 2011, *Sci*, **333**, 1121
- Peplowski, P. N., Evans, L. G., Hauck, S. A., et al. 2011, *Sci*, **333**, 1850
- Peplowski, P. N., Klima, R. L., Lawrence, D. J., et al. 2016, *NatGe*, **9**, 273
- Peplowski, P. N., Lawrence, D. J., Evans, L. G., et al. 2015, *P&SS*, **108**, 98
- Plainaki, C., Mura, A., Milillo, A., et al. 2017, *JGRE*, **122**, 1217
- Plane, J. M. C. 2012, *ChSRv*, **41**, 6507
- Pokorný, P. 2018, *ApJ*, **863**, 31
- Pokorný, P., & Kuchner, M. 2019, *ApJL*, **873**, L16
- Pokorný, P., Mazarico, E., & Schorghofer, N. 2021, *PSJ*, **2**, 85
- Pokorný, P., Sarantos, M., & Janches, D. 2017, *ApJL*, **842**, L17
- Pokorný, P., Vokrouhlický, D., Nesvorný, D., Campbell-Brown, M., & Brown, P. 2014, *ApJ*, **789**, 25
- Porubcan, V., Kornos, L., & Williams, I. P. 2006, *CoSka*, **36**, 103
- Reach, W. T., Kelley, M. S., & Sykes, M. V. 2007, *Icar*, **191**, 298
- Rennilson, J. J., & Criswell, D. R. 1974, *Moon*, **10**, 121
- Sachse, M., Schmidt, J., Kempf, S., & Spahn, F. 2015, *JGRE*, **120**, 1847
- Sarantos, M., Killen, R. M., McClintock, W. E., et al. 2011, *P&SS*, **59**, 1992
- Sasaki, S., & Kurahashi, E. 2004, *AdSpR*, **33**, 2152
- Sasaki, S., Kurahashi, E., Yamanaka, C., & Nakamura, K. 2003, *AdSpR*, **31**, 2537
- Sasaki, S., Nakamura, K., Hamabe, Y., Kurahashi, E., & Hiroi, T. 2001, *Natur*, **410**, 555
- Selsis, F., Brillet, J., & Rapaport, M. 2004, *A&A*, **416**, 783
- Soja, R. H., Grün, E., Strub, P., et al. 2019, *A&A*, **628**, A109
- Soja, R. H., Sommer, M., Herzog, J., et al. 2015a, *A&A*, **583**, A18
- Soja, R. H., Herzog, J. T., Sommer, M., et al. 2015b, in *Proc. Int. Meteor Conference*, ed. J.-L. Rault & P. Roggemans (Mechelen: IMO), 66
- Solomon, S. C., McNutt, R. L., Gold, R. E., & Domingue, D. L. 2007, *SSRv*, **131**, 3
- Solomon, S. C., Nittler, L. R., & Anderson, B. J. 2018, *Mercury: The View after MESSENGER* (Cambridge: Cambridge Univ. Press)
- Sommer, M., Yano, H., & Srama, R. 2020, *A&A*, **635**, A10
- Spahn, F., Sachse, M., Sei?, M., et al. 2019, *SSRv*, **215**, 11
- Speyerer, E. J., Povilaitis, R. Z., Robinson, M. S., Thomas, P. C., & Wagner, R. V. 2016, *Natur*, **538**, 215
- Srama, R., Ahrens, T. J., Altobelli, N., et al. 2004, *SSRv*, **114**, 465
- Srama, R., Kempf, S., Moragas-Klostermeyer, G., et al. 2011, *CEAS*, **2**, 3
- Sremcevic, M., Krivov, A. V., & Spahn, F. 2003, *P&SS*, **51**, 455
- Stenborg, G., Gallagher, B., Howard, R. A., Hess, P., & Raouafi, N. E. 2021, *ApJ*, **910**, 157
- Stenborg, G., Stauffer, J. R., & Howard, R. A. 2018, *ApJ*, **868**, 74
- Sterken, V. J., Westphal, A. J. N. A. D. M., & F, P. 2019, *SSRv*, **215**, 43
- Stöffler, D., Gault, D. E., Wedekind, J., & Polkowski, R. 1975, *JGR*, **80**, 4042
- Strom, R. G. 1979, *SSRv*, **24**, 3
- Strub, P., Krüger, H., & Sterken, V. J. 2015, *ApJ*, **812**, 140
- Strub, P., Sterken, V. J., Soja, R., et al. 2019, *A&A*, **621**, A54
- Sykes, M. V., & Greenberg, R. 1986, *Icar*, **65**, 51
- Sykes, M. V., Lebofsky, L. A., Hunten, D. M., & Low, F. 1986, *Sci*, **232**, 1115
- Sykes, M. V., & Walker, R. G. 1992, *Icar*, **95**, 180
- Szalay, J. R., & Horanyi, M. 2015a, *GeoRL*, **42**, 10,580
- Szalay, J. R., & Horanyi, M. 2015b, *GeoRL*, **42**, 5141
- Szalay, J. R., & Horanyi, M. 2016a, *GeoRL*, **43**, 4893
- Szalay, J. R., & Horanyi, M. 2016b, *ApJL*, **830**, L29
- Szalay, J. R., & Horanyi, M. 2020, *ApJL*, **901**, L19
- Szalay, J. R., Pokorný, P., Bale, S. D., et al. 2020, *ApJS*, **246**, 27
- Szalay, J. R., Pokorný, P., Horanyi, M., et al. 2019, *P&SS*, **165**, 194
- Szalay, J. R., Pokorný, P., Malaspina, D. M., et al. 2021, *PSJ*, **2**, 185
- Szalay, J. R., Poppe, A. R., Agarwal, J., et al. 2018, *SSRv*, **214**, 98
- Thompson, M. S., Loeffler, M. J., Morris, R. V., Keller, L. P., & Christoffersen, R. 2019, *Icar*, **319**, 499
- Thompson, M. S., Morris, R. V., Clemett, S. J., et al. 2020, *Icar*, **346**, 113775
- Thompson, M. S., Zega, T. J., Becerra, P., Keane, J. T., & Byrne, S. 2016, *M&PS*, **51**, 1082
- Thompson, M. S., Vander Kaaden, K. E., Loeffler, M. J., & McCubbin, F. M. 2021, *LPSC*, **52**, I496
- Trang, D., Gasda, P. J., Corley, L. M., Gillis-Davis, J. J., & Lucey, P. G. 2018, *LPSC*, **49**, 2083
- Trang, D., Lucey, P. G., & Izenberg, N. R. 2017, *Icar*, **293**, 206
- Vander Kaaden, K. E., & McCubbin, F. M. 2015, *JGRE*, **120**, 195
- Vander Kaaden, K. E., McCubbin, F. M., Nittler, L. R., et al. 2017, *Icar*, **285**, 155
- Vervack, R. J., McClintock, W. E., Killen, R. M., et al. 2010, *Sci*, **329**, 672
- Veverka, J., Thomas, P. C., Robinson, M., et al. 2001, *Sci*, **292**, 484
- Wang, X., Schwan, J., Hsu, H. W., Grün, E., & Horanyi, M. 2016, *GeoRL*, **43**, 6103
- Wehry, A., Krüger, H., & Grün, E. 2004, *A&A*, **419**, 1169
- Weider, S. Z., Nittler, L. R., Starr, R. D., McCoy, T. J., & Solomon, S. C. 2014, *Icar*, **235**, 170
- Weider, S. Z., Nittler, L. R., Starr, R. D., et al. 2015, *E&PSL*, **416**, 109
- Whipple, F. L. 1940, *PAPhS*, **83**, 711
- Witte, M. 2004, *A&A*, **426**, 835
- Wood, B. E., Müller, H.-R., & Witte, M. 2015, *ApJ*, **801**, 62
- Wurz, P., Fatemi, S., Galli, A., et al. 2022, *SSRv*, **218**, 10
- Yamada, M., Sasaki, S., & Nagahara, H. 1999, *EP&S*, **51**, 1255
- Yang, K., Schmidt, J., Feng, W., & Liu, X. 2022, *A&A*, **659**, A120
- Zaslavsky, A., Mann, I., Soucek, J., et al. 2021, *A&A*, **656**, A30